Draft version April 21, 2021
Typeset using LaTeX **twocolumn** style in AASTeX631

A 'Quick Look' at All-Sky Galactic Archeology with TESS: 130,000 Oscillating Red Giants from the MIT Quick-Look Pipeline

Marc Hon,[1,2,*] Daniel Huber,[1] James S. Kuszlewicz,[3] Dennis Stello,[2,4,5,6] Jamie Tayar,[1,*] Joel C. Zinn,[7,2,†] Mathieu Vrard,[8] and Marc H. Pinsonneault[8]

[1] *Institute for Astronomy, University of Hawai'i, 2680 Woodlawn Drive, Honolulu, HI 96822, USA*
[2] *School of Physics, The University of New South Wales, Sydney NSW 2052, Australia*
[3] *Landessternwarte, Zentrum für Astronomie der Universität Heidelberg, Königstuhl 12, 69117, Heidelberg, Germany*
[4] *ARC Centre of Excellence for Astrophysics in Three Dimensions (ASTRO-3D), Australia*
[5] *Stellar Astrophysics Centre, Department of Physics and Astronomy, Aarhus University, Ny Munkegade 120, DK-8000 Aarhus C, Denmark*
[6] *Sydney Institute for Astronomy (SIfA), School of Physics, University of Sydney, NSW 2006, Australia*
[7] *Department of Astrophysics, American Museum of Natural History, Central Park West at 79th Street, New York, NY 10024, USA*
[8] *Department of Astronomy, The Ohio State University, Columbus, OH 43210, USA*

ABSTRACT

We present the first all-sky yield of oscillating red giants from the prime mission data of NASA's Transiting Exoplanet Survey Satellite (TESS). We apply a combination of supervised and unsupervised machine learning techniques towards long-cadence TESS photometry from the first data release by the MIT Quick-Look Pipeline to detect the presence of red giant oscillations in frequency power spectra. The detected targets are conservatively vetted to produce a final list of 129,323 oscillating red giants. Although this list approximates a lower bound to the possible yield of oscillating giants across TESS's nominal mission, it is a one order of magnitude increase over the yield from *Kepler* and *K2*. We report surface temperature and *Gaia*-derived radius measurements for each detected target as well as estimates of their frequency at maximum oscillation power. Using our measurements, we present the first near all-sky *Gaia*-asteroseismology mass map, which shows global structures consistent with the expected stellar populations of our Galaxy. In addition, we examine the spatial, kinematic, and chemical properties of our red giant sample to demonstrate the strong potential of TESS asteroseismology for studies of the Galaxy even with only one month of observations.

Keywords: asteroseismology — stars: oscillations — methods: data analysis

1. INTRODUCTION

With high-precision, uninterrupted photometry from previous space-borne missions CoRoT (Baglin et al. 2006), *Kepler* (Borucki et al. 2010) and *K2* (Howell et al. 2014), red giant asteroseismology has emerged as a powerful tool for probing stellar populations around the Milky Way. The precise measurements of masses, radii, and ages across thousands of field red giants offered by asteroseismology has brought forth new avenues for detailed studies of Galactic archeology whereby such measurements are combined with kinematic and spectroscopic information to build a map describing the chemical and dynamical evolution of the Milky Way (e.g., Miglio et al. 2013; Casagrande et al. 2016; Silva Aguirre et al. 2018; Sharma et al. 2019; Miglio et al. 2021).

However, efforts to apply asteroseismology across the Galaxy have been mainly hampered by the size of the observing windows provided by previous space missions. CoRoT observed a number of 4 square degree fields focused towards two opposite directions, providing seismic detections for ∼3,000 giants (de Assis Peralta et al. 2018). Meanwhile, *Kepler* observed one region in the northern hemisphere spanning 100 square degrees, which resulted in ∼20,000 detections (Hon et al. 2019). The *K2* mission observed 18 '*Kepler* field'-sized regions along the

Corresponding author: Marc Hon
mtyhon@hawaii.edu

* NASA Hubble Fellow
† NSF Astronomy and Astrophysics Postdoctoral Fellow.

ecliptic, motivating the establishment of the *K2* Galactic archeology Program (Stello et al. 2017; Zinn et al. 2020), which will further increase the number of detections by ∼30,000 (Zinn et al., in review). Now, we seek to extend the scope of red giant asteroseismology towards the entire sky with NASA's Transiting Exoplanet Survey Satellite (Ricker et al. 2014, TESS). Throughout the first two years of its nominal mission, TESS surveyed nearly the entire sky by observing 13 distinct sectors in both northern and southern hemispheres. Each sector covers a 96°x 24° field of view and yields Full Frame Images (FFIs) that provide high-precision flux measurements of millions of stars for up to 27 days at a 30-minute cadence. This unprecedented level of sky coverage is expected to increase the number of red giants with detected oscillations by about an order of magnitude over its predecessors.

A big challenge faced by asteroseismology with TESS is the survey's observational duration. The majority of targets from the first two years of TESS observations will only be observed for a month, resulting in lower frequency resolution compared to *Kepler* and *K2*. However, the asteroseismic inference of stellar populations using TESS data is still viable. Depending on the availability of precise seismic measurements, Silva Aguirre et al. (2020) showed that it is possible to obtain precision levels of up to ∼3% for radii, ∼5% for mass, and ∼20% for ages when incorporating both spectroscopy and parallax information in modelling the brightest ($V \sim 6-7$) TESS red giants. Similar precision levels were found by Stello et al. (in prep.) when comparing seismic results from TESS data against those from 4-year *Kepler* data for ∼2,000 red giants observed in both *Kepler* and TESS. Furthermore, Mackereth et al. (2021) recovered median mass uncertainties of ∼ 8% and age uncertainties of ∼ 26% for ∼1,700 red giants with $G < 11$ near the southern ecliptic pole, where FFI targets were observed by TESS for up to a year. Mackereth et al. (2021) additionally indicate that the seismic ages of giants from TESS are sufficiently precise to distinguish chemically- and kinematically-defined structures within the Milky Way disk. Although the current outlook for red giant asteroseismology with TESS is promising, it has yet to be extended to the majority of TESS FFI targets. Not only is this because significantly more effort is required to systematically detect populations of oscillating red giants across the millions of TESS FFI targets, but detailed seismic parameters like the large frequency separation are difficult to measure with one-month long observations (Mackereth et al. 2021, Stello et al. in prep.). The frequency at maximum oscillation power, $\nu_{\rm max}$, however, can be measured from any star with a detected oscillation power excess, making it a more accessible seismic measurement for inferring fundamental stellar properties.

The systematic detection of red giant oscillations, which has previously posed a significant challenge in the field, can now be facilitated using machine learning algorithms (Hon et al. 2018b, 2019). Such tools are vital in the era of TESS given the enormous volume of data the mission will provide, and indeed particular emphasis on the analyses of TESS-like datasets in asteroseismic machine learning has been provided in recent work (e.g., Armstrong et al. 2016; Hon et al. 2018a; Bugnet et al. 2019; Kgoadi et al. 2019; Kuszlewicz et al. 2020; Audenart et al. in prep.). However, an important aspect of supervised learning — which comprise most of current machine learning algorithms in asteroseismology — is the presence of training data that is expected to be representative of the data upon which inference is to be performed. In comparison to *Kepler* and *K2*, TESS has photometric qualities and instrumental noise sources that are unique to its observing instrument. This property makes it challenging to generalize algorithms that learn from *Kepler*/*K2* data towards TESS data.

Despite these challenges, we proceed with applying machine learning to perform the first all-sky detection of red giants across the full two-year TESS Primary Mission. We examine all light curves that have been extracted from FFIs by the MIT Quick-Look Pipeline (Huang et al. 2020a,b, QLP) as High Level Science Products. In conjunction with detecting a substantial number of oscillating TESS red giants, we also provide a 'first look' at TESS's asteroseismic potential for full-sky Galactic archeology.

2. DATA

We use all FFI light curves from the QLP team's first data release[1], which comprises observations across Sectors 1-26. This data release includes all targets brighter than a TESS magnitude of 13.5 and contains 24,376,080 light curves that have an observing cadence of ∼30 minutes. In this study, we use only the 'raw' light curves obtained using simple aperture photometry (`SAP_FLUX`). We do not use the detrended light curves (`KSPSAP_FLUX`), which are optimized for planet searches and therefore have stellar variability over long timescales filtered out. Additionally, we only use timestamps with a good quality flag (`QUALITY=0`). Next, we high-pass filter each light curve using a boxcar filter with a width of 2-days and compute the light curve's power

[1] https://archive.stsci.edu/hlsp/qlp/

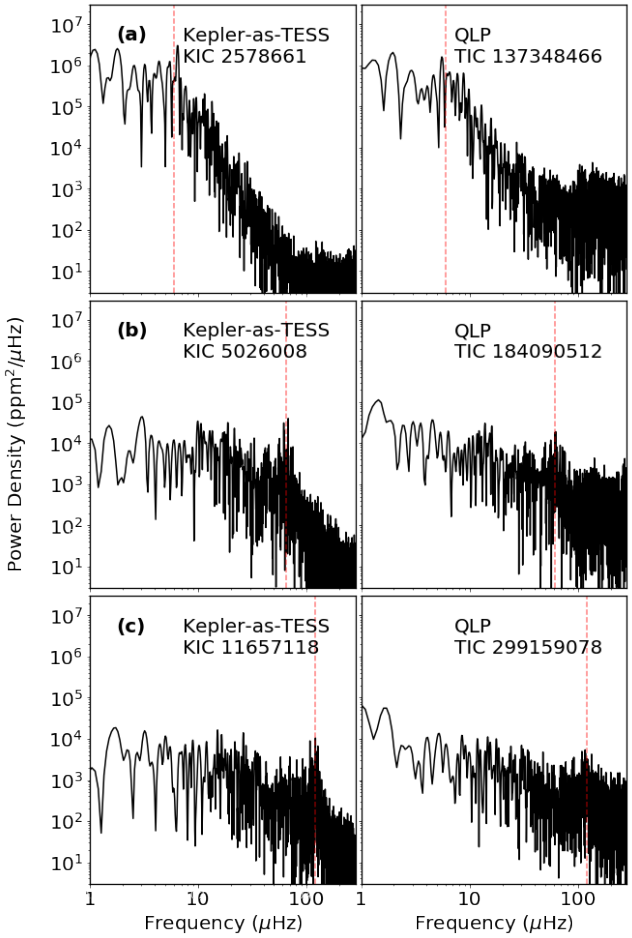

Figure 1. A comparison of red giant frequency power spectra from *Kepler* and TESS. Each row corresponds to a red giant oscillating at a specific $\nu_{\rm max}$ value (red line). Power spectra in the left column correspond to 27-day light curves from *Kepler*, while those in the right column correspond to the same *Kepler* targets but observed by TESS.

spectral density using the generalized Lomb-Scargle periodogram (Lomb 1976; Scargle 1982). During this processing, we exclude light curves which have most ($\geq 95\%$) of their timestamps empty, resulting in a total of 23,962,744 power spectra corresponding to 14,702,113 unique stars observed by TESS[2].

3. METHOD

3.1. *Neural Networks*

We use the deep learning method as described by Hon et al. (2018b) to 'visually' detect the presence of red giant oscillations within frequency power spectra. In particular, two convolutional neural networks are applied towards 2D images of log-log[3] power spectra. By binning each star's power spectrum into a 128x128 binary image, the first neural network outputs a classification score, $p_{\rm det}$, between 0 and 1 indicating the likelihood that red giant oscillations are visible within the spectrum. The second network, which trained independently from the first, is a regression network that measures the frequency at maximum oscillation power, $\nu_{\rm max}$ and its corresponding uncertainty, $\sigma_{\nu_{\rm max}}$. Specific details of the structure of both networks are provided in Appendix A.

3.2. *Training Data*

To train and test the classifier, we use KEPSEISMIC[4] light curves (Mathur et al. 2019) of 196,581 *Kepler* targets of which 21,914 were identified to be oscillating red giants from the detections provided by Hon et al. (2019). For the $\nu_{\rm max}$ regression network, we use a subset of the oscillating giants, specifically 16,194 red giants that have $\nu_{\rm max}$ values measured from the asteroseismic data pipeline by Yu et al. (2018). For both classification and regression datasets, we allocate 70% of data to be used for training, 15% to be used to internally validate and tune the network, and the remaining 15% for network testing, which we describe in Section 3.3.

Because we want to train the deep learning method on light curves of comparable duration to TESS data, each 4-year light curve in the training sets is segmented into multiple, unique 27-day segments. Due to the decrease of S/N with shorter time series as well as the stochastic behaviour of solar-like oscillations, there is, however, no guarantee that oscillations detectable in a 4-year light curve will be visible over its constituent 27-day light curve segments. Using 4-year $\nu_{\rm max}$ measurements from Yu et al. (2018), we apply the formalism of Chaplin et al. (2011) to statistically assess the significance of the oscillations within $\pm 0.66\ \nu_{\rm max}^{0.88}$ around $\nu_{\rm max}$ for the power spectrum of each 27-day light curve segment[5]. For a power spectrum of a light curve segment to be included in the training set, it must have an oscillation SNR exceeding the 1% false alarm threshold of a pure white noise spectrum. Because the $\nu_{\rm max}$ for each power spectrum is already known from 4-year *Kepler* data, we measure the oscillation SNR directly from the spectrum rather than estimating it fundamental stellar properties

[2] A fraction of targets are observed in multiple TESS sectors within overlapping fields of view, resulting in more power spectra than unique stars within the data release.

[3] The power spectra are represented in log-frequency on the x-axis and log-power density on the y-axis.

[4] https://archive.stsci.edu/prepds/kepseismic/

[5] Following Mosser et al. (2012), this frequency range is approximately twice the full width at half maximum of the oscillation power envelope.

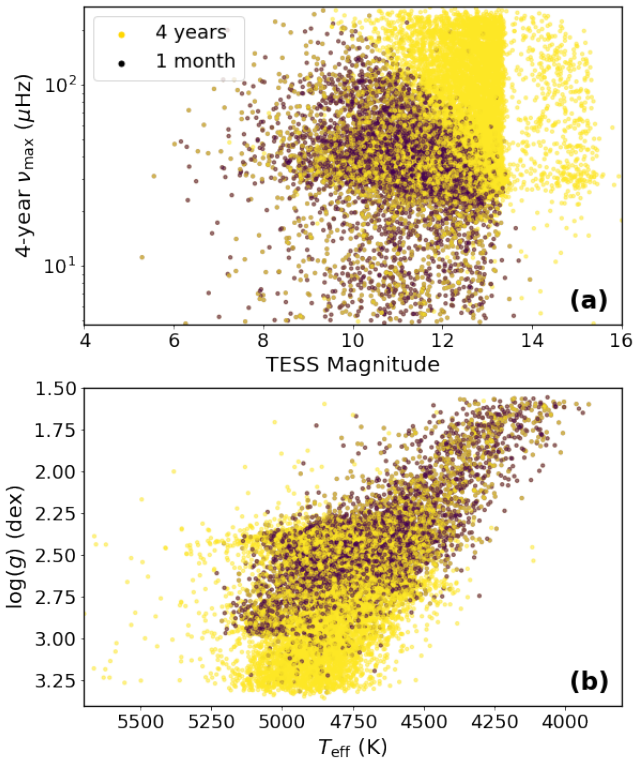

Figure 2. The estimated difference in yield for oscillating *Kepler* red giants between 4-year *Kepler* data and 1-month TESS data, depicted with a ν_{max}-magnitude diagram in panel (a) and a Kiel diagram in panel (b). The ν_{max} and log(g) values shown here are from Yu et al. (2018), while the estimate for the 1-month yield is calculated following the Chaplin et al. (2011) formalism for predicting seismic yields.

as per the original Chaplin et al. (2011) approach. We determine white noise levels for this assessment from the properties of *Kepler* long-cadence photometry as documented by Jenkins et al. (2010). Our final classification training set comprising *Kepler* data contains 714,820 light curves showing red giant oscillations and 4,959,892 light curves without red giant oscillations. Meanwhile, there are a total of 550,786 red giant power spectra for training the ν_{max} regression network.

One major challenge with using our *Kepler* training set is its difference in photometric data quality compared to TESS. Besides differences in instrumental noise, TESS observations have lower photometric precision levels and are more susceptible to crowding effects due to its larger pixels. Power spectra from TESS data are therefore expected to have greater noise levels compared to *Kepler* data that we use for training, as demonstrated in Figure 1. As a result, the visibility of the oscillations for low luminosity (high ν_{max}) red giants, particularly for those at the red giant branch, are diminished when approaching fainter TESS magnitudes as shown in Figure Figure 2a. Here, it can be seen that for TESS magnitudes $\gtrsim 10$, high ν_{max} oscillations that can be seen with 4 years of data are not expected to be observed in 1 month of data. Consequently, we expect to detect oscillations primarily in giants with $\log(g) \gtrsim 3.0$ dex as shown in Figure 2b.

Besides the expected yield, the difference in photometric data quality between *Kepler* and TESS will also affect how well our networks can perform; it is thus important to identify this difference in performance so that we can determine a decision threshold that can adequately recover oscillating giants from TESS data.

3.3. *Setting a Network Decision Threshold*

3.3.1. *Classification Thresholds*

Figure 3a demonstrates how changing the acceptance threshold for the classifier affects the sample completeness and purity of the resulting oscillating giant yield of our 27-day *Kepler* test data. Sample completeness reports the fraction of true oscillating giants within the test data that are successfully recovered by the classifier, while sample purity reports the fraction of accepted test stars that are truly oscillating giants. A lower acceptance threshold, p_{thresh}, accepts more targets and thus has greater completeness but at the cost of lower purity (more false positives). Conversely, a higher p_{thresh} may miss a greater number of genuinely oscillating giants (lower completeness) but is less likely to admit false positives. Indeed, Figure 3b shows that a strict threshold of $p_{thresh} = 0.95$ significantly reduces the false positive rate across all magnitudes in the test set. Because we expect raw QLP light curves to contain greater white noise levels and uncorrected instrumental noise than our *Kepler* test set, we choose to be conservative in accepting positive detections and thus adopt $p_{thresh} = 0.95$.

To assess how greater noise levels from TESS will affect our ability to detect oscillations, we evaluate the classifier's completeness on synthetic TESS-like light curves created using `celerite`[6], which models stochastic variability in astrophysical time series using Gaussian processes. Artificial red giant light curves are generated using current information available about oscillation mode parameters and the granulation background. The granulation background emulates 'model F' from Kallinger et al. (2014) with parameter values derived from the scaling relations found therein. The red giant universal pattern (Mosser et al. 2011) is used to gener-

[6] https://celerite.readthedocs.io/

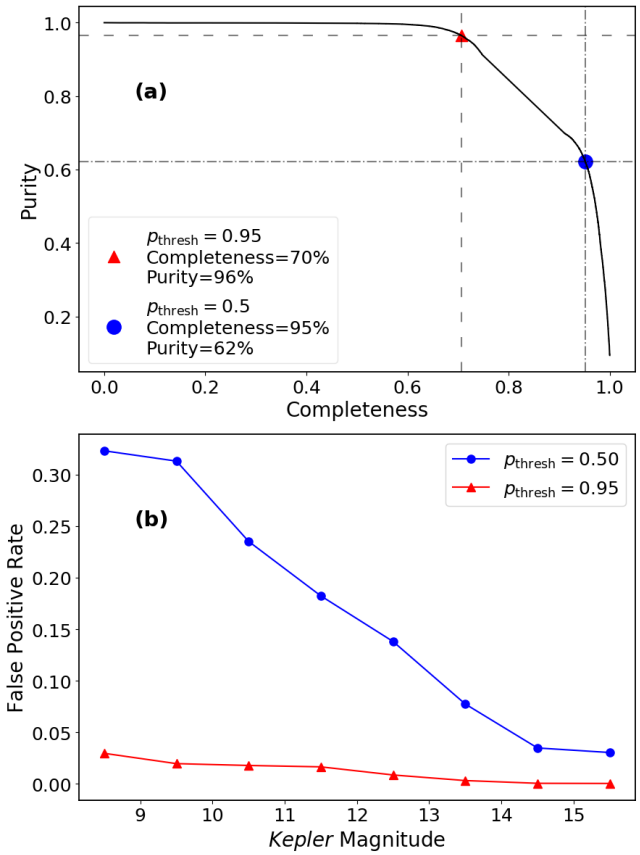

Figure 3. Performance of the classifier network on 27-day *Kepler* test data. (a) Purity-completeness curves for different acceptance thresholds of the network. Two particular thresholds are highlighted: a default threshold of $p_{\rm thresh} = 0.5$ and a stricter threshold of $p_{\rm thresh} = 0.95$ that we adopt in this study. (b) False positive rate as a function of *Kepler* magnitude for different $p_{\rm thresh}$. The decrease towards fainter magnitudes suggests that most false positives in this test set are not from pure white noise spectra, but from spectra containing signals from other forms of variability like binarity or rotation, which can confuse the classifier.

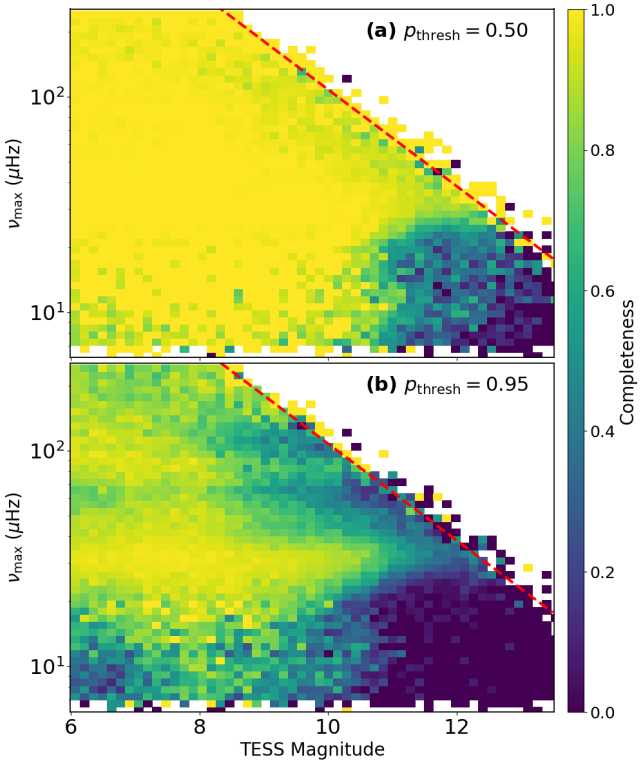

Figure 4. Completeness of the classifier on a test set of synthetic TESS red giants. (a) The recovery rate of oscillating red giants as a function of TESS magnitude and $\nu_{\rm max}$ when using an acceptance threshold, $p_{\rm thresh} = 0.5$. (b) Similar to panel (a) but with $p_{\rm thresh} = 0.95$. The red line in each panel delineates the boundary of the test set defined as where the height of the oscillation power excess is equal to ten times the white noise level in the power spectra.

ate frequencies of $\ell = 0, 2, 3$ oscillation modes from a given $\nu_{\rm max}$ value, with amplitudes estimated from the scaling relations given in Mosser et al. (2012) and the mixed $\ell = 1$ oscillation modes computed according to the formalism by Vrard et al. (2016) and Mosser et al. (2018). Because the mixed mode parameters depend on red giant evolutionary states, we determine evolutionary states for a synthetic red giant with a given $\nu_{\rm max}$ by sampling from a known $\nu_{\rm max}$-dependent distribution of known *Kepler* red giant evolutionary states (Elsworth et al. 2019). Next, we convert all derived oscillation parameters into the parameterization accepted by the simple harmonic oscillator kernel in `celerite` following Pereira et al. (2019) and subsequently generate light curves of 27-day duration. To mimic the TESS observing window, we include a 1-day gap in the middle of the light curve, which simulates the data downlink event. Finally, we add white noise into the light curves following the TESS long-cadence noise properties described by Sullivan et al. (2015), where we assume observations with no instrumental noise contribution and an ecliptic latitude of 30°. Examples of simulated power spectra are shown in Appendix B.

We simulate light curves across a uniform $\nu_{\rm max}$ range of [5, 250] μHz and a uniform TESS magnitude range of [6.0, 13.5] at the same time. Figure 4 shows the completeness of the classifier on a synthetic test set of 152,520 TESS red giants, where we can observe the performance of the network across a range of magnitudes and $\nu_{\rm max}$. As expected, the overall completeness of the yield reduces with a stricter $p_{\rm thresh}$, but there are several detection biases that can now be identified:

- The completeness remains high across all magnitudes for stars with $30\mu{\rm Hz} \leq \nu_{\rm max} \leq 40\mu{\rm Hz}$, indicating that oscillations representative of stars at

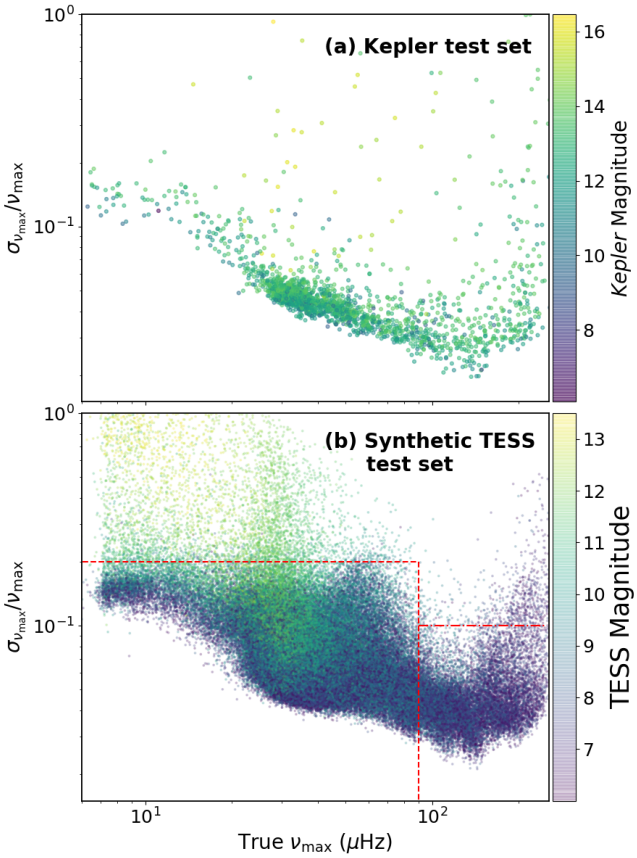

Figure 5. (a) The distribution of estimated fractional uncertainties of the $\nu_{\rm max}$ regression network for the *Kepler* red giant test set, which comprises 15% of the 16,194 red giants analyzed by Yu et al. (2018) as described in Section 3.2. (b) Same as panel (a) but for the simulated TESS test set. The red lines delineate boundaries that we use to indicate a confident estimate of $\nu_{\rm max}$.

or near the red clump are easier to detect by the method. This bias is likely the result of having an over-representation of such stars relative to other giants in our *Kepler* training set.

- A relatively low completeness across all magnitudes for stars with $\nu_{\rm max} \lesssim 20\mu$Hz. Oscillations within this frequency regime have an envelope width spanning fewer frequency bins, which makes the visual identification of the power excess in a log-log power spectrum difficult. This relation of network performance to frequency resolution can also be seen in *Kepler* data (c.f. Hon et al. 2019, their Figure 3). Due to the greater frequency resolution of 4-year *Kepler* data, the regime of low detection probability only occurs at $\nu_{\rm max} \lesssim 15\mu$Hz in the Hon et al. (2019) analysis.

- A low completeness for the faint and luminous giants, i.e., stars with TESS magnitudes fainter than 11 and $\nu_{\rm max} \lesssim 25\mu$Hz. This observation suggests that for low $\nu_{\rm max}$ stars, an important indicator of an oscillating giant to the classifier is the visibility of the granulation profile in power spectra, i.e., red noise. As a result, the network is significantly less confident in its estimate for low $\nu_{\rm max}$ stars when the power spectrum is dominated by white noise and has a flat frequency-power profile. Appendix C discusses this aspect further with an example.

3.3.2. *Regression Threshold*

Additionally, we set a criterion based on the properties of the $\nu_{\rm max}$ regression network, which is trained independently of the classifier. Figure 5 shows a comparison of fractional $\nu_{\rm max}$ uncertainties from the network across the *Kepler* (real) and TESS-like (simulated) test sets in this study. The uncertainties shown for the *Kepler* test set represent the best-case scenario for the network because the $\nu_{\rm max}$ regression network is trained on *Kepler* data. Results on the synthetic test set, which has a broader range of white noise levels compared to its *Kepler* counterpart, show a broader scatter of uncertainties — this includes a larger upwards scatter for fainter targets with $\nu_{\rm max} \lesssim 25\mu$Hz that we associate with the network's inability to locate a distinct oscillation power excess for such stars. We therefore determine a piecewise boundary (in red) below which we consider the network's $\nu_{\rm max}$ estimate to be consistent with a correct identification of an oscillation power excess. This boundary preserves over 96% of the test set estimates in Figure 5 and is described by $\sigma_{\nu_{\rm max}}/\nu_{\rm max} = 20\%$ for $\nu_{\rm max} < 90\mu$Hz and $\sigma_{\nu_{\rm max}}/\nu_{\rm max} = 10\%$ for $\nu_{\rm max} \geq 90\mu$Hz.

3.3.3. *Threshold Summary*

The combined criteria that we use in our networks are as follows:

- $p_{\rm det} \geq 0.95$ from the classifier.
- $\sigma_{\nu_{\rm max}}/\nu_{\rm max} \leq 20\%$ for stars with $\nu_{\rm max} < 90\mu$Hz.
- $\sigma_{\nu_{\rm max}}/\nu_{\rm max} \leq 10\%$ for stars with $\nu_{\rm max} \geq 90\mu$Hz.

These criteria are heuristic approaches that prioritize the *purity* of the detection yield using our methods. We apply these concessions because we aim to report the highest quality detections from TESS QLP data to cater towards optimizing early spectroscopic follow-up across both northern and southern hemispheres of the sky.

Importantly, our reported results do not represent a complete population of all oscillating giants from TESS FFIs. To properly assess the completeness of our networks in detecting oscillating giants, we require more principled approaches to calibrating decision thresholds

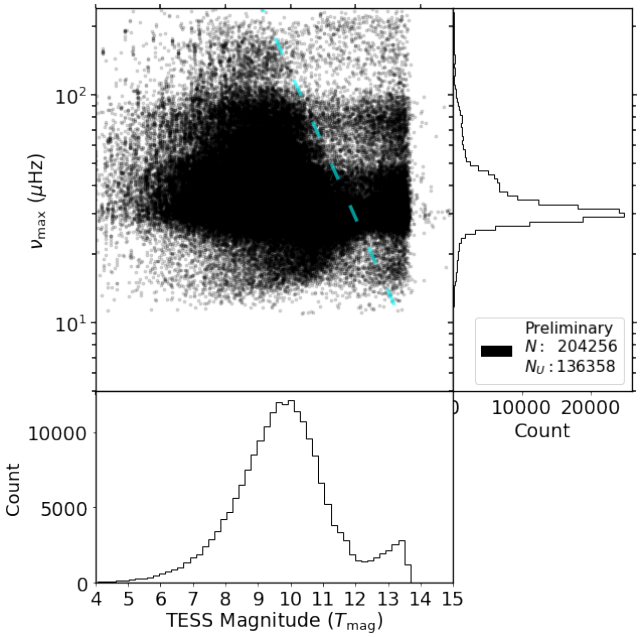

Figure 6. ν_{max}-magnitude distribution of all targets in the low luminosity sample. The number N corresponds to the number of individual light curves whose power spectra show red giant oscillations, while the number N_U corresponds to the total number of unique oscillating giants. The dashed blue line delineates a magnitude-dependent boundary above which the density of detected giants diminishes significantly and is identified as the oscillation detection limit. This limit is more clearly defined in Figure 8b.

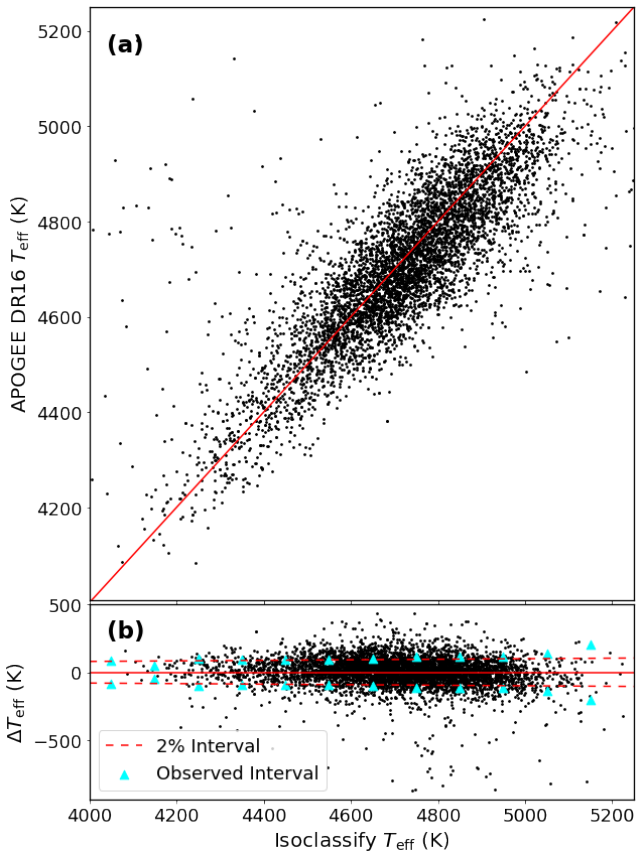

Figure 7. (a) A comparison between spectroscopic temperatures from APOGEE DR16 with the values measured in this work for 5,699 targets in our final yield in Section 5. The red line indicates the one-to-one relation. For visual clarity, we do not show outliers whose temperatures differences are beyond the 99.7th percentile range within this set of targets. (b) Residual differences in temperature defined as ΔT_{eff} = (`isoclassify` T_{eff} − APOGEE DR16 T_{eff}). The dashed lines delineate a 2% interval range representing the adopted `isoclassify` T_{eff} uncertainties. The cyan points delineate the observed uncertainty interval by calculating the dispersion of the residuals across different T_{eff} values.

by benchmarking our networks on real, labeled TESS data. Such a dataset has yet to be made because the systematic differences in photometric data quality between TESS and *Kepler* have yet to be fully quantified, in addition to the recency of FFI light curves extracted in bulk. We thus defer the analysis of sample completeness to a forthcoming paper.

4. SEISMIC DETECTION

4.1. *Low Luminosity Sample*

Figure 6 shows the detection result from our neural networks comprising 136,358 unique FFI targets that meet the threshold criteria outline in Section 3.3. The number of detected oscillating giants declines at TESS magnitudes (T_{mag}) fainter than 10 as a result of white noise levels beginning to limit the detection of oscillations from giants with the lowest luminosities (highest ν_{max}) within our sample. However, the quantity of detected giants begins to artificially increase for $T_{mag} \gtrsim 12$ due to the presence of blended targets, namely faint non-red giants whose light curves show red giant oscillations due to flux contamination ('blending') from neighbouring giants. Due to the large TESS pixels, blending is expected to be particularly problematic for the detection task for fainter giants; its onset in Figure 6 is estimated to be between $T_{mag} \sim 11 - 12$.

4.1.1. *Effective Temperatures and Radii*

To eliminate blended targets, we require that each target has a surface temperature (T_{eff}) and radius (R) that is representative of an oscillating red giant. We calculate these stellar parameters for each target in our preliminary yield using the 'direct method' of the `isoclassify`[7] stellar classification code (Huber et al. 2017; Berger et al. 2020). The code uses parallaxes from

[7] https://github.com/danxhuber/isoclassify

Gaia EDR3 (Gaia Collaboration et al. 2020) as an input. These parallaxes are first corrected for zero-point offsets following the prescription by Lindegren et al. (2020), which applies corrections to stars with five- and six-parameter astrometric solutions. For stars brighter than a *Gaia* magnitude of 10.8 that are corrected by the five-parameter offset model, we further subtract 0.015mas from their corrected parallaxes following the recommendation by Zinn (2021), who identified that the zero-point model over-corrects the *Gaia* parallaxes for such stars through a comparison with *Kepler* targets with known asteroseismic parallaxes. Using these corrected parallaxes, we then calculate distance posteriors using an exponentially decreasing volume density prior with a length scale of 1.35 kpc (Bailer-Jones 2015; Astraatmadja & Bailer-Jones 2016).

We then calculate extinction values, A_V, for each star using the combined 3D dust maps of Drimmel et al. (2003), Marshall et al. (2006), and Green et al. (2019) from the `mwdust` repository[8](Bovy et al. 2016), where we assume an extinction uncertainty of 0.02 mag. These extinction values are applied to 2MASS K band magnitudes to calculate apparent magnitudes. Bolometric corrections are inferred by interpolating $T_{\rm eff}$, $\log g$, [Fe/H], and A_V in the MESA Isochrones and Stellar Tracks (Choi et al. 2016) bolometric correction tables (MIST/C3K, Conroy et al., in prep[9]), where we adopt an absolute solar bolometric magnitude of 4.74 mag, as appropriate to reproduce solar values for the bolometric corrections in the MIST grid. These bolometric corrections, which have an assumed uncertainty of 0.02 mag, are applied to the apparent magnitudes to derive absolute magnitudes and subsequently values of luminosities, L. Using 2MASS JHK photometry, we apply the infrared flux method-based color-$T_{\rm eff}$ relations from González Hernández & Bonifacio (2009) to infer values of $T_{\rm eff}$. Finally, we use L and $T_{\rm eff}$ to estimate R using the Stefan-Boltzmann relation.

A comparison between our temperature measurements with those from APOGEE Data Release 16 spectroscopy (Majewski et al. 2017, DR16) in Figure 7a shows good levels of agreement and additionally demonstrates that the residual dispersion between both temperature sources are generally at the 2% level (Figure 7b). We therefore approximate $\sigma_{\rm T_{eff}}$ as 2% of the reported $T_{\rm eff}$ value. Meanwhile, output estimates for distances, L and R are reported as their distribution median values from Monte-Carlo sampling, with 1σ confidence intervals de-

[8] https://github.com/jobovy/mwdust

[9] http://waps.cfa.harvard.edu/MIST/model_grids.html

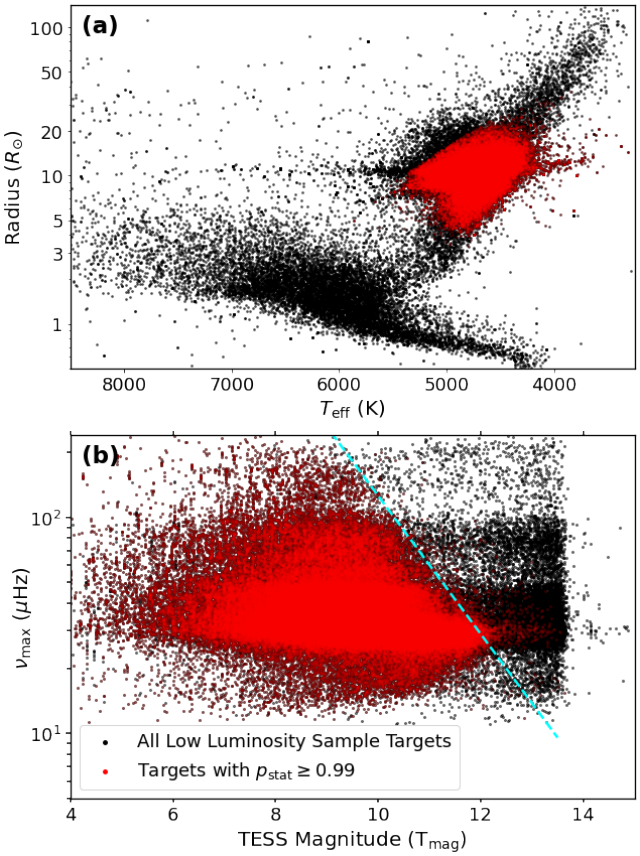

Figure 8. (a) Radius-temperature plot of all targets in the low luminosity sample (black) and remaining targets after retaining only those with $p_{\rm stat} \geq 0.99$. (b) The $\nu_{\rm max}$-magnitude distribution of the stars in panel (a). The detection limit first seen in Figure 6 (blue line) is now clearly seen after the application of a $p_{\rm stat} \geq 0.99$ threshold. The black points shown here are the same as those shown in Figure 6.

rived from distribution percentiles. Fractional uncertainty estimates are typically 4% for L and 5% for R. With these fundamental stellar parameters, we now proceed with the analysis of the low luminosity sample.

4.1.2. *Removing Blended Targets*

Having measured $T_{\rm eff}$ and R for each target in our low luminosity sample, we calculate their statistical detection probabilities, $p_{\rm stat}$, using the Chaplin et al. (2011) global SNR estimation approach that has been adapted to TESS following the modifications described by Campante et al. (2016) and Schofield et al. (2019). More specifically, asteroseismic scaling relations are used to predict oscillation and granulation amplitudes (Chaplin et al. 2011; Kallinger et al. 2014) from $T_{\rm eff}$ and R, while contributions from white noise and instrumental effects are estimated following the TESS instrumental specifications by Sullivan et al. (2015). These quantities are used to estimate the SNR of oscillations in a power

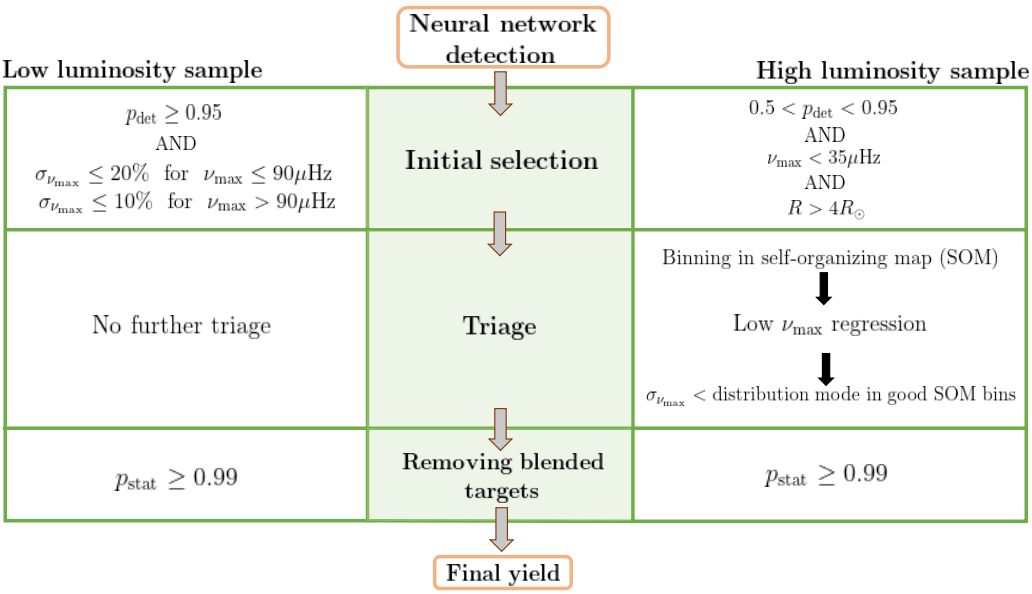

Figure 9. A flowchart outlining the steps to vet the two samples of oscillating TESS red giants reported by this study. The low luminosity sample, described in Section 4.1, passes the network threshold criteria determined in Section 3.3 and is filtered by their Chaplin et al. (2011) probability, $p_{\rm stat}$. The high luminosity sample (Section 4.2) are low $\nu_{\rm max}$ stars that do not meet the network threshold criteria but are vetted using a self-organizing map and also filtered by $p_{\rm stat}$.

spectrum and subsequently $p_{\rm stat}$. The value $p_{\rm stat}$ indicates the probability that the oscillation SNR exceeds a particular threshold, which — following Campante et al. (2016)— is the SNR at which there exists a 5% chance the detected oscillation signal arises from noise alone. Crucially, $p_{\rm stat}$ is a simple prediction of how likely oscillations can be observed for a given TESS target using only its fundamental stellar parameters and survey properties (e.g., apparent magnitude, observing cadence); it therefore does not directly use information from the observed power spectra of each target. As a result, our neural network detection algorithm is still needed to directly confirm the presence of visible oscillations from the observed data. Nonetheless, $p_{\rm stat}$ removes most of the obvious blends from our neural network detections. In particular, $p_{\rm stat}$ is small ($\ll 0.99$) for detected targets that either have $T_{\rm eff}$ and R that are not representative of a red giant or TESS magnitudes too faint to expect detectable red giant oscillations.

When calculating $p_{\rm stat}$, we assume that each target experiences no blending (hence a flux dilution factor of 1) and a negligible systematic noise level ($\sigma_{\rm sys} = 0$). However, we do take into account the positional dependence of the background noise across the sky. To be conservative, we enforce a threshold of $p_{\rm stat} \geq 0.99$, which as shown in Figure 8a, removes all blended targets and false positives within the instability strip (i.e., hot classical pulsators) and on the main sequence (dwarf stars). The $\nu_{\rm max}$-magnitude plot in Figure 8b shows that removing these false positives reveals a distinct boundary (blue line), which we parameterize as $\nu_{\rm max} = 10^{-0.32T_{\rm mag}} + 5.3$. We interpret this boundary as the oscillation detection limit above which white noise levels are too high for oscillations to be detectable. Filtering using $p_{\rm stat}$ additionally reveals a deficiency of $p_{\rm stat} \geq 0.99$ targets with $\nu_{\rm max} \lesssim 25\mu$Hz and $T_{\rm mag} \gtrsim 11.5$ in Figure 8b. This suggests that the non-filtered targets (black points) previously occupying that region in $\nu_{\rm max}$-magnitude space are actually blended stars and are not genuinely faint and luminous giants. We note that this observed lack of faint and luminous giants is consistent with the limitations of our classifier as discussed in Section 3.3. The remaining stars after the $p_{\rm stat}$ filtering comprises our final low luminosity sample, with several examples of these stars documented in Appendix D.

4.2. *High Luminosity Sample*

A key observation from Figure 6 is the lack of stars with $\nu_{\rm max} \lesssim 25\mu$Hz, which is a result of having strong detection thresholds from both the classifier and $\nu_{\rm max}$ regression network as detailed in Section 3.3. Instead of discarding all targets that do not pass the detection thresholds, we attempt to recover a sizeable population of luminous giants as described in this section. We begin by identifying 147,318 stars with an estimated $\nu_{\rm max} < 35\mu$Hz that have $0.5 < p_{\rm det} < 0.95$ — these are thus excluded from the low luminosity sample. Next, we identify oscillations within the high luminosity sample

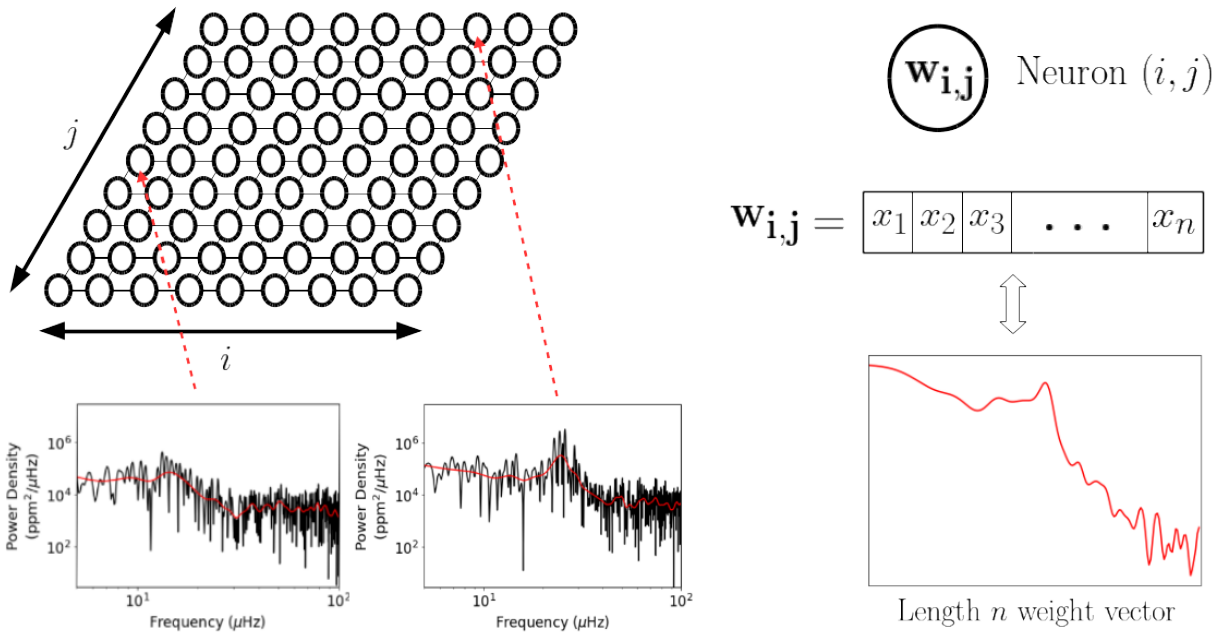

Figure 10. Schematic of the self-organizing map (SOM) used in this work. Here, the SOM is a 9×9 grid of neurons, where each neuron comprises a weight vector $\mathbf{w}$ of length of $n = 200$ that acts as a template spectrum. The weight vector of each neuron is trained to match specific patterns of the logarithmic frequency-power profiles of power spectra (smooth red curves), which also have a length of $n = 200$. As depicted by the red arrows, power spectra are assigned towards distinct regions of the map depending on the shape of their frequency-power profile.

through two additional methods: binning with a self-organizing map (Kohonen 1982, SOM) and by low $\nu_{\rm max}$ regression. We outline a summary of how both 'low luminosity' and 'high luminosity' samples are defined in Figure 9.

4.2.1. *Self-Organizing Map*

The SOM is an unsupervised learning approach using artificial neural networks that projects data into a discrete, low-dimensional representation while preserving similarity relations between data samples. As depicted in Figure 10, the input to the SOM comprises log frequency-log power spectra between the range of [5, 100] μHz with log power density normalized to zero mean and unit variance. The power spectra are then smoothed using a Gaussian filter with a width of 15 frequency bins and binned into an array of length 200. The discrete, low-dimensional representation corresponds to a 9×9 grid of neurons, where each neuron comprises a weight vector that is also of length 200 that can be thought of as a template spectrum. The smoothed power spectrum of a star will be assigned to a particular neuron on the grid if the spectrum has the smallest Euclidean distance to template of that neuron. The training objective of a SOM is to iteratively adjust the weight vector of each neuron to form better matching templates to the patterns shown by power spectra. We describe the training process more mathematically in Appendix E. Different power spectra are assigned to different neurons on the grid because the SOM uses a 'winner-take-all' approach where neurons at different grid positions learn to match different patterns. As a result, the SOM learns to associate similarity in patterns with relative positions within the grid. In other words, our two-dimensional neuron grid forms a topographic map where stars with similar power spectra are clustered in the same region on the map.

We use the SOM implementation by `MiniSom`[10] (Vettigli 2018) to map all power spectra in the high luminosity sample into a 9×9 neuron grid as shown in the left panel of Figure 11. The SOM enables us to easily select groups of stars that show visible oscillations (green tick) and those that do not (red cross). While there are some neurons with templates without a significantly visible power excess (such as those at positions (4,6) and (7,7)), there are also a few with a power excess only marginally visible (such as neurons at positions (2,7) and (7,5)). We visually inspect the power spectra assigned to each 'marginal' neuron and find that most have low S/N with traces of a power excess only under heavy smoothing of the spectrum. In the interest of selecting only stars with distinctly visible oscillations, we reject stars assigned to these marginal neurons. Although this vetting process

[10] https://github.com/JustGlowing/minisom

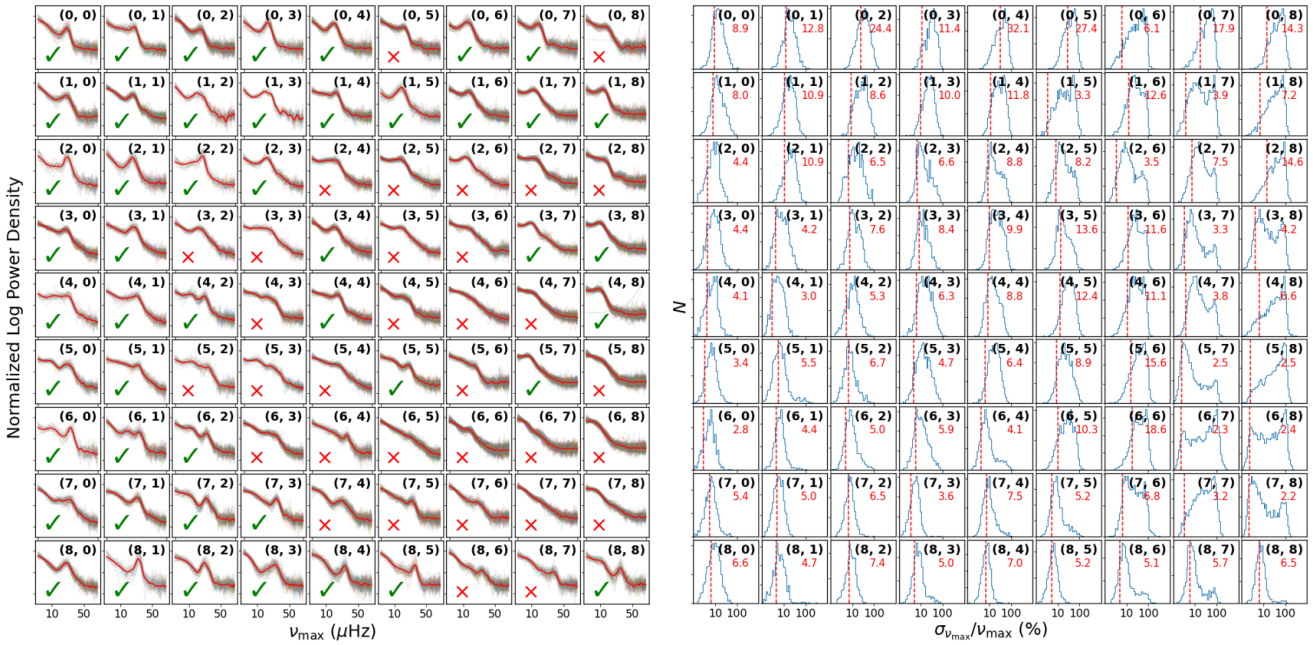

Figure 11. (Left) The self-organizing map applied to the power spectra of stars in the high luminosity sample, with each panel representing a map position. Stars are assigned to different regions of the map based on the frequency-power profile of their power-normalized log-log power spectra, which are represented by the gray curves in each panel. The red curve in each panel corresponds to the template spectrum of a neuron at that map position, which is conceptually similar to the average of all power spectra assigned to that particular neuron. The ticks or crosses indicate which neuron templates we accept or reject on the basis of whether or not their power spectra clearly show oscillations. (Right) The fractional uncertainty of the frequency at maximum power, $\sigma_{\nu_{\rm max}}$, of stars assigned to each neuron on the map as estimated by the low $\nu_{\rm max}$ regression network (see text). The vertical line in each panel indicates the $\sigma_{\nu_{\rm max}}$ distribution mode, with the number in red reporting the corresponding mode value.

is subjective, our main Galactic archeology results for the high luminosity sample in Section 6.2 do not significantly change with slight differences in SOM neuron selection. Importantly, our selection mainly retains targets whose power spectrum very distinctly shows an oscillation power excess and a granulation background, some of which are shown in Appendix D.

4.2.2. *Low $\nu_{\rm max}$ regression*

Because the $\nu_{\rm max}$ regression network introduced in Section 3 is not precise for luminous giants (particularly for faint targets, see Figure 4), we train a new regression network specifically for stars with $\nu_{\rm max} \leq 35\mu$Hz. The main difference between this new network compared to the previous is the data representation used, which we alter to now only span the limited frequency range of [5, 100] μHz. Additionally, this network is trained on a synthetic training set comprising 45,838 `celerite` light curves that have $\nu_{\rm max}$ uniformly distributed between 5 and 35μHz, and TESS magnitudes between 6 and 13.5. We posit that this new regression network measures $\nu_{\rm max}$ for luminous giants more reliably than the previous network for two reasons. First, the new network examines a narrower range of frequencies in power spectra such that its optimization is now significantly more focused towards estimating low $\nu_{\rm max}$ values precisely. Secondly, although the synthetic data lacks instrumental noise inherent to real TESS observations it contains a more diverse range of white noise levels — the lack of which is a major drawback in the old training set as discussed in Section 2. We apply the low $\nu_{\rm max}$ regression network to all stars in the high luminosity sample and examine the resulting estimate uncertainties in each SOM bin as shown in Figure 11. As expected, we find that bins with larger variations in $\sigma_{\nu_{\rm max}}$ correlate with bins that contain lower $\nu_{\rm max}$ power spectra. Again, we choose to be conservative with our selection by retaining only stars whose $\sigma_{\nu_{\rm max}}$ are below the most common value, hence the mode of the $\sigma_{\nu_{\rm max}}$ distribution, in each bin.

4.2.3. *Removing Blended Targets and Final High Luminosity Sample*

Using the same methods in Sections 4.1.1 and 4.1.2, we determine $T_{\rm eff}$ and R for the resulting high luminosity sample and retain only stars with $p_{\rm stat} \geq 0.99$. Figure 12a shows that our resulting high luminosity sample adds more giants with $R \gtrsim 10 R_\odot$ to the total detections in this work, which corresponds to stars with $\nu_{\rm max} \lesssim 25\mu$Hz in Figure 12b. The lack of faint giants,

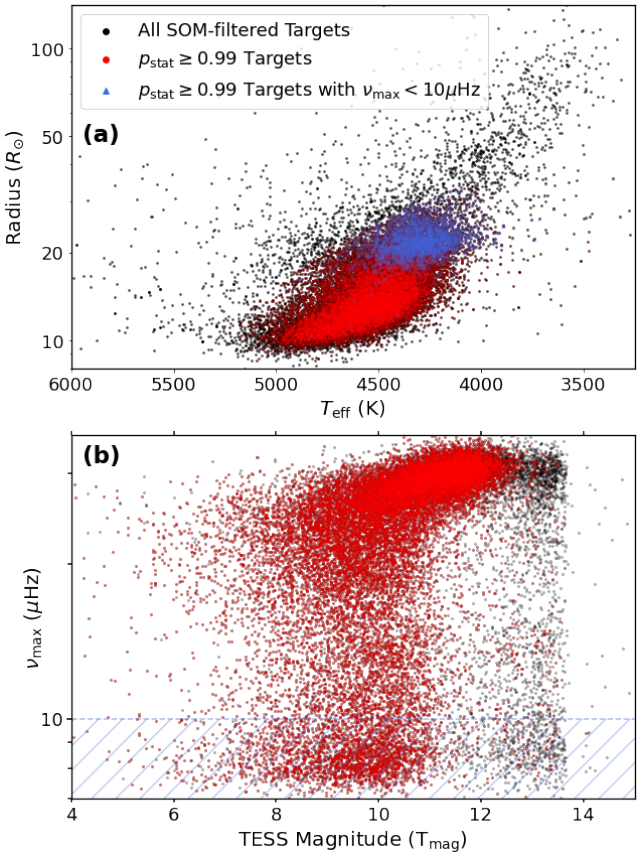

Figure 12. (a) Radius-temperature plot of the high luminosity sample after SOM vetting (black) and the sample after retaining only targets with $p_{\rm stat} \geq 0.99$ (red). The blue points are $p_{\rm stat} \geq 0.99$ targets that we do *not* include in our final high luminosity yield because they have too low $\nu_{\rm max}$ values (see text). (b) The $\nu_{\rm max}$-magnitude relation for the high luminosity sample. The red points within the blue hatched region are those shown in blue in panel (a).

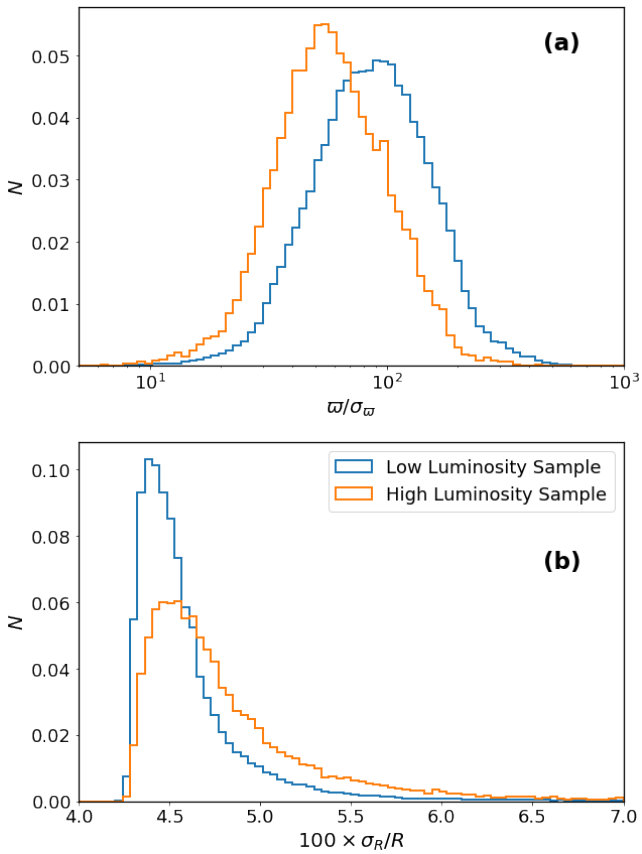

Figure 13. (a) The distribution of parallax over uncertainty (ϖ/σ_ϖ) for each final sample reported. The fraction of stars with $\varpi/\sigma_\varpi < 10$ is 0.07% for the low luminosity sample and 0.23% for the high luminosity sample. (b) The distribution of fractional radius uncertainty for each final sample. Typical radius uncertainties are 4.4% for the low luminosity sample and 4.5% for the high luminosity sample.

particularly at TESS magnitudes fainter than 11, indicates that our SOM approach also struggles to recover faint and luminous giants. It is nonetheless an improvement over the classifier network because a fraction of faint, low $\nu_{\rm max}$ stars are now retained instead of being completely filtered out.

We observe an overdensity of stars with $\nu_{\rm max} \lesssim 10\mu$Hz (hatched region in Figure 12b). One possible explanation for this feature is that we are detecting giants that are in the asymptotic giant bump, which has similarly been identified by Mackereth et al. (2021) for TESS CVZ stars. Another possibility is that we may be misidentifying other types of long period variability such as binarity or blending from γ Doradus variables as low $\nu_{\rm max}$ oscillations. With only one month of observation, distinguishing between these variability types from their low frequency peaks in power spectra is inherently difficult. Because we are not confident in our ability to distinguish the type of variability shown by these targets, we do not include stars with an estimated $\nu_{\rm max} \leq 10\mu$Hz in our final reported sample. We do, however, list these stars in Appendix F because some may be useful candidates for follow-up studies of binary stars or long period variables observed by TESS.

5. FINAL YIELD

5.1. *Target Lists*

Table 1 lists 113,187 unique targets comprising the final low luminosity sample together with their measured parameters in this study. Table 2 presents the equivalent for the high luminosity sample's final sample of 16,136 unique targets. We present each sample in separate ta-

Table 1. List of 113,187 unique TESS targets comprising the final low luminosity sample. Included are each target's TESS magnitude (Tmag), its estimated frequency at maximum oscillation power ($\nu_{\rm max}$), and measurements of surface temperature ($T_{\rm eff}$), radii (R), luminosity (L), and distances (d). Values of the re-normalized unit weight error (`ruwe`) from *Gaia* EDR3 (Gaia Collaboration et al. 2020) are included to flag potential non-single sources whose astrometric solutions may be problematic for the analysis in Section 6. Values of `mass_flag` are binary indicators of whether the target's stellar mass as estimated using the seismic scaling relation (Equation 1) are within the 'typical' mass range of a red giant from *Kepler* (see text). The full version of this table is available in a machine-readable format in the online journal, with a portion shown here for guidance regarding its form and content.

TIC	$\nu_{\rm max}$ (μHz)	$T_{\rm mag}$ (mag)	$T_{\rm eff}$ (K)	R ($R_\odot$)	L ($L_\odot$)	d (kpc)	`ruwe`	`mass_flag`
1078	30.8 ± 2.2	9.7	4629 ± 92	11.3 ± 0.5	52.6 ± 2.3	0.828 ± 0.012	1.21	1
2026646	47.0 ± 5.6	12.8	4415 ± 88	16.3 ± 1.2	90.1 ± 11.0	4.249 ± 0.250	0.95	0
31635521	112.1 ± 6.1	7.6	4909 ± 98	6.4 ± 0.3	21.5 ± 0.7	0.212 ± 0.001	1.10	1
51931461	69.8 ± 4.0	9.3	4803 ± 96	8.2 ± 0.4	32.4 ± 2.1	0.554 ± 0.015	4.43	1
150440218	87.5 ± 5.4	10.4	4815 ± 96	6.2 ± 0.3	18.8 ± 0.7	0.699 ± 0.005	0.97	1
...	...	...	...	...	...	...	...	...

Table 2. Same as Table 1, but for the final high luminosity sample comprising 16,136 unique sources.

TIC	$\nu_{\rm max}$ (μHz)	$T_{\rm mag}$ (mag)	$T_{\rm eff}$ (K)	R ($R_\odot$)	L ($L_\odot$)	d (kpc)	`ruwe`	`mass_flag`
10675	26.7 ± 1.6	10.4	4829 ± 96	10.3 ± 0.5	51.5 ± 2.4	1.122 ± 0.019	1.02	1
5454859	12.7 ± 0.7	10.3	4230 ± 84	17.7 ± 0.9	90.5 ± 5.2	1.405 ± 0.031	1.03	1
19020780	31.3 ± 2.3	12.2	4327 ± 86	14.0 ± 0.8	61.6 ± 5.5	2.378 ± 0.095	1.44	1
342179989	15.9 ± 0.9	11.3	4704 ± 94	11.2 ± 0.5	55.5 ± 2.6	1.564 ± 0.027	0.91	0
411973673	10.1 ± 0.4	12.9	4400 ± 88	20.4 ± 1.8	139.4 ± 21.8	3.060 ± 0.195	1.16	1
...	...	...	...	...	...	...	...	...

bles because each have been vetted by different methods and combining samples will thus complicate our understanding of the selection biases within each method. In each table, we report $\nu_{\rm max}$ measurements for only one sector for targets with multi-sector detections. For the final low luminosity sample, we find that 96% of $\nu_{\rm max}$ measurements across individual sectors of the same star deviate less than 2σ of the quoted uncertainties in Table 1. For the final high low luminosity sample, 72% of similar measurements are within the quoted 2σ uncertainties in Table 2 — as further elaborated in Section 5.3, we attribute this lower precision to the differences in approach between samples. In total, our yield from this study comprises 129,323 oscillating giants; we consider the size of this sample to be a lower bound estimate of the yield of oscillating giants across TESS's nominal mission because of the conservative measures we have used in both detection and vetting methods. In comparison to the predicted all-sky yield of $\sim 3 \times 10^5$ as reported by Mackereth et al. (2021), our current yield suggests that there are still many giants that can potentially be detected from TESS. We defer more extensive detections across TESS FFIs to address population completeness in future work.

Although we have used measurements of $T_{\rm eff}$ and R to filter out obvious blends in each final sample, such an approach cannot discern the occurrence of blending when both target and blending star are red giants. To potentially identify such scenarios, we include the *Gaia* re-normalized unit weight error (Lindegren 2018, `ruwe`) and `mass_flag` parameters in both Tables 1 and 2. Values of `ruwe`> 1.40 for a target indicate that the adopted astrometric solution is less likely to be reliable due to neighbouring sources, and is thus a useful way for

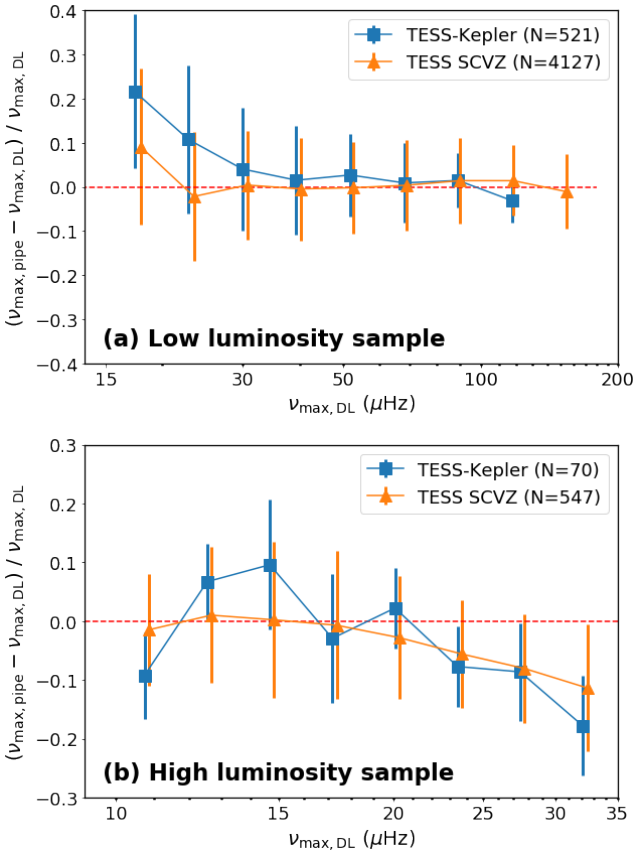

Figure 14. (a) The fractional differences of our frequency at maximum oscillation power measurements ($\nu_{\rm max,DL}$) with those from asteroseismic data pipelines ($\nu_{\rm max,pipe}$) for stars in the final low luminosity sample that are also in the *Kepler* field of view (Stello et al. in prep., TESS-*Kepler*), and for those also in the Southern Continuous Viewing Zone (Mackereth et al. 2021, TESS-SCVZ). The number N indicates the total number of stars in each comparison, while the errorbars indicate the binned combined $\nu_{\rm max}$ uncertainties. (b) Same as panel (a) but for the high luminosity sample.

identifying targets with potential companions that cause blending (e.g., Evans 2018; Belokurov et al. 2020). The `mass_flag` value indicates whether or not the asteroseismic scaling mass (M) for each target falls within the 'typical' mass range of a red giant. We estimate masses using the following formula:

$$\frac{M}{M_\odot} = \left(\frac{\nu_{\rm max}}{\nu_{\rm max,\odot}}\right)\left(\frac{R}{R_\odot}\right)^2\left(\frac{T_{\rm eff}}{T_{\rm eff,\odot}}\right)^{0.5}, \quad (1)$$

with $\nu_{\rm max,\odot} = 3090\mu$Hz (Huber et al. 2011) and $T_{\rm eff,\odot} = 5772$K (Prša et al. 2016). Equation 1 is the seismic $\nu_{\rm max}$ scaling relation that relates the acoustic cutoff frequency of a star to its M, R, and $T_{\rm eff}$ (Brown et al. 1991; Kjeldsen & Bedding 1995; Belkacem et al. 2011).

We define the typical mass range of a red giant to be the values between the 0.5$^{\rm th}$ and 99$^{\rm th}$ percentile of ∼16,000 *Kepler* red giant masses as measured by Yu et al. (2018), which corresponds to the interval $0.6M_\odot \geq M \geq 2.9M_\odot$. Stars within this range are given `mass_flag`=1, while those outside the interval (`mass_flag`=0) are flagged as having an outlier mass value. We do not exclude these targets from our list because there are rare circumstances under which such extreme mass measurements can occur (such as a $3M_\odot$ giant), but we caution that many of these are likely blends.

5.2. *Measurement Consistency*

In Figure 13a, we show the uncertainty distribution for the parallaxes that we use to derive radii measurements for each sample. Given that our samples probe a relatively local region of the Galaxy (as further discussed in Section 6), the vast majority of our detected targets have precise astrometric measurements that result in a typical fractional radius uncertainty of 4.5% as shown in Figure 13b. The difference in parallax precision between these two samples is caused by the stars in the high luminosity sample typically being located at farther distances compared to those in the low luminosity sample.

In Figure 14, we compare our $\nu_{\rm max}$ measurements from Tables 1 and 2, $\nu_{\rm max,DL}$, with those from asteroseismic data pipelines, $\nu_{\rm max,pipe}$, which are based on independent studies of TESS targets in specific sky regions. The first comparison is for targets in the *Kepler* field of view based on the analysis by Stello et al. (in prep.), while the second comparison is for targets in the TESS Southern Continuous Viewing Zone (TESS SCVZ) that comprise the 'gold' sample based on the analysis by Mackereth et al. (2021). Figure 14a shows that $\nu_{\rm max,DL}$ is in good agreement with $\nu_{\rm max,pipe}$ for $\nu_{\rm max,DL} \gtrsim 25\mu$Hz. Below this range, $\nu_{\rm max,DL}$ appears to be systematically underestimated by about 1σ compared to $\nu_{\rm max,pipe}$, which is consistent with our findings in Section 3.3 indicating that our neural networks have greater difficulties in detecting and estimating the seismic properties of such low $\nu_{\rm max}$ stars. The comparison with the high luminosity sample (Figure 14b), however, shows the opposite trend where $\nu_{\rm max,DL}$ is systematically overestimated for $\nu_{\rm max,DL} \gtrsim 25\mu$Hz while being consistent with $\nu_{\rm max,pipe}$ for values between ∼10-20μHz.

5.3. *Caveats*

There are several important additional caveats that should be considered with the current target lists:

- Blending may still be prevalent especially when both the target and blending star have $\nu_{\rm max}$ values comparable to one another. We recommend

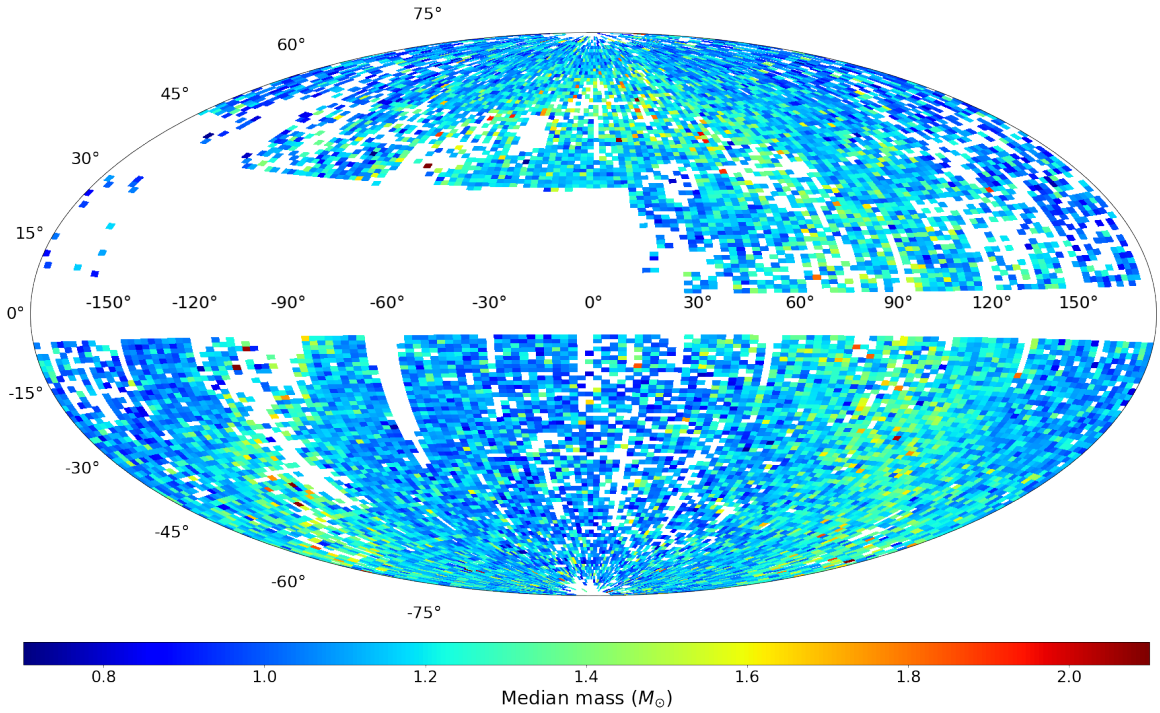

Figure 15. All-sky *Gaia*-asteroseismology mass map of stars in the low luminosity sample with `ruwe` ≤ 1.40 and `mass_flag` $= 1$ plotted in ecliptic coordinates. There are 150 bins across each dimension (longitude and latitude), with bins having fewer than 3 stars excluded. The missing patches of sky in the northern hemisphere correspond to Sectors 14-16 and 24-26, during which TESS's boresight was shifted towards higher ecliptic latitudes to avoid excessive stray Earth- and moonlight.

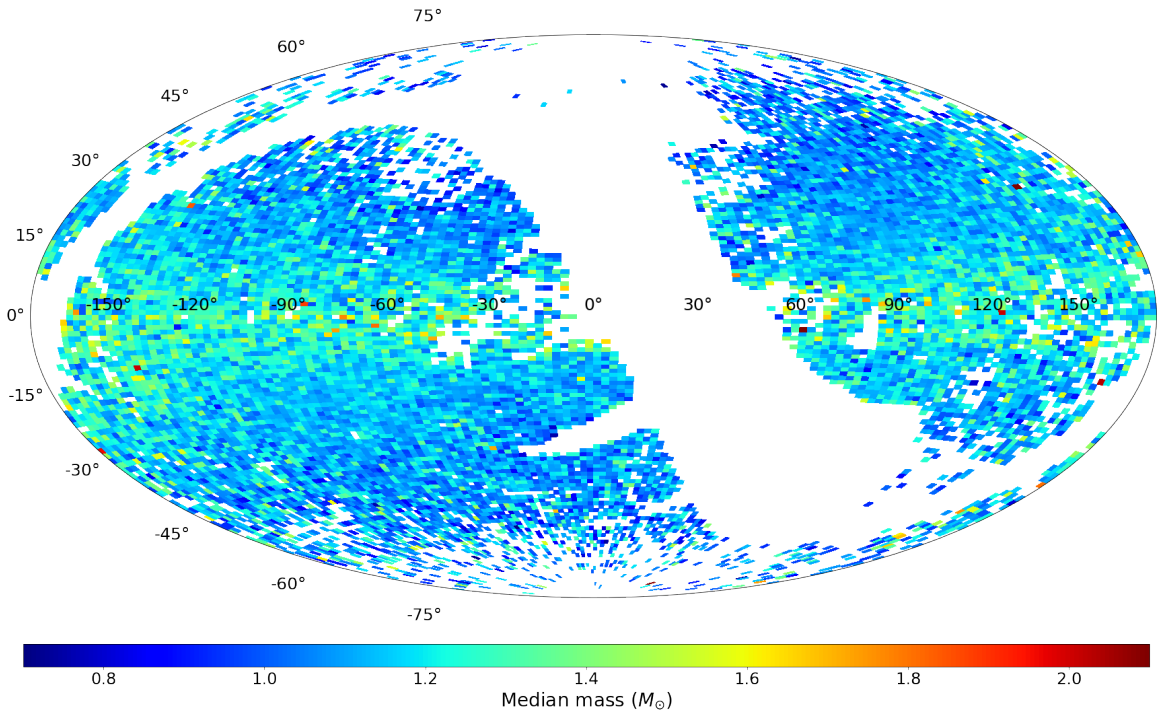

Figure 16. Same as Figure 15, but using the Galactic coordinate system (l, b).

more caution with the fainter targets ($T_{\rm mag} \sim 12$) in our sample as well as those located closer to the Galactic plane, where crowding effects become more problematic. One approach that can inform the presence of blending, which we will explore in future work, is to systematically determine a contamination/crowding metric calculated from the aperture of each target. Another possible method to identify giant-giant blending would be to determine if the stellar mass as estimated from Equation 1 (which uses *Gaia*-derived radii) is consistent with a mass determined from the combined $\Delta\nu$-$\nu_{\rm max}$ scaling relation (e.g., Pinsonneault et al. 2018, Equation 4), where $\Delta\nu$ is the large frequency separation of the oscillation modes.

- The selection for the final yield of the high luminosity sample is performed by visual inspection facilitated by unsupervised learning (i.e., the SOM). Therefore, the sample is considered to be coarsely vetted, which makes it possible that stars with spurious signals that appear as oscillations can make it through the vetting process. Furthermore, $\nu_{\rm max}$ estimates for the sample are based on a regression network trained only on simulated data. By keeping in mind that simulated data does not factor in potential systematic noise sources in real data, it is likely that $\sigma_{\nu_{\rm max}}$ is underestimated for a fraction of high luminosity stars. We therefore advise readers to be conservative when considering the $\nu_{\rm max}$ estimates for this sample.

- The search performed in this study is not intended to be exhaustive, meaning that there are potentially many more oscillating giants from TESS that are yet to be detected. In the interest of producing an early, all-sky catalogue comprising strong candidates of oscillating giants, we make concessions to the population completeness of our final sample by vetting our preliminary yield with several thresholds. Because these thresholds are conservative, the number of remaining stars is expected to be a reasonable approximation of the minimum yield of oscillating giants that we can observe across the first two years of TESS.

6. POTENTIAL FOR GALACTIC STUDIES

6.1. *Low Luminosity Sample Results*

In this section, we demonstrate the prospects of the detected giants from this study towards studies of the Milky Way, which aims to show the utility of our yield for target selection in large-scale spectroscopic surveys and provide an astrophysical validation of the accuracy of our results. We include only the 103,076 oscillating giants with `ruwe` ≤ 1.40 and `mass_flag` $= 1$ to minimize the effect of blending in the following demonstrations.

In Figures 15 and 16, we show all-sky Hammer map projections of the final yield of the low luminosity sample, colored by seismic scaling masses derived using Equation 1. Given that red giants follow an age-mass relation (e.g., Miglio 2011; Bellinger 2020), our results show that younger stars (higher mass stars) are mainly confined to the plane of the Galactic disc, i.e., the equator in Figure 16, with older stars (lower mass stars) generally populating higher Galactic latitudes. Notably, these trends are broadly consistent with global age trends obtained from all-sky spectroscopic surveys (Xiang et al. 2017; Sanders & Das 2018). At $|l| \lesssim 120°$ in Figure 16, we note a slight trend of higher mass stars towards higher latitudes, which may indicate the presence of disk flaring (e.g., Mackereth et al. 2017).

Next, we investigate the spatial extent of our sample by calculating Galactocentric coordinates $(X_{\rm Gal}, Y_{\rm Gal}, Z_{\rm Gal}, R_{\rm Gal})$ using the `Galactocentric` module from Astropy (Astropy Collaboration et al. 2018), which assumes the Sun's distance from the Galactic center to be 8.122 kpc and the Sun's height above the Galactic plane to be 20.8 pc. Figures 17a and 17b show that the majority of stars have $|R_{\rm Gal,\odot} - R_{\rm Gal}| < 1$ kpc and $|Z_{\rm Gal,\odot} - Z_{\rm Gal}| < 1$ kpc, indicating that we mainly probe stars that are relatively near to us compared to *Kepler* (e.g., Rodrigues et al. 2014; Mathur et al. 2016) or *K2* (e.g., Rendle et al. 2019). This result is expected given that the focus of the TESS mission is primarily on nearby, bright stars, and that our current yield is limited to TESS magnitudes below 13.5. Figure 17b distinctly shows a gradient of mass as a function of $Z_{\rm Gal}$, which we further visualize in the right panel of the same figure. This observation suggests a vertical mass gradient of the Milky Way disk similar to that found by Casagrande et al. (2016), which indicates the possibility of our yield to probe the mass and age structure of the Galactic disk in detail.

To examine the kinematic properties of our yield, we use parallaxes, radial velocities, and proper motions from *Gaia* EDR3 to determine Galactocentric velocities $V = (V_X, V_Y, V_Z)$. Figure 18a visualizes the resulting kinematic space with a Toomre diagram — a useful representation for differentiating Galactic populations based on their kinematics (e.g., Venn et al. 2004). We observe that most stars have $V_Y \sim 200 - 250$ km/s, which is approximately the circular velocity of the Local Standard of Rest (LSR, e.g., Ding et al. 2019). In other words, most stars have velocities that are typical to objects orbiting the Milky Way within the disk. Fol-

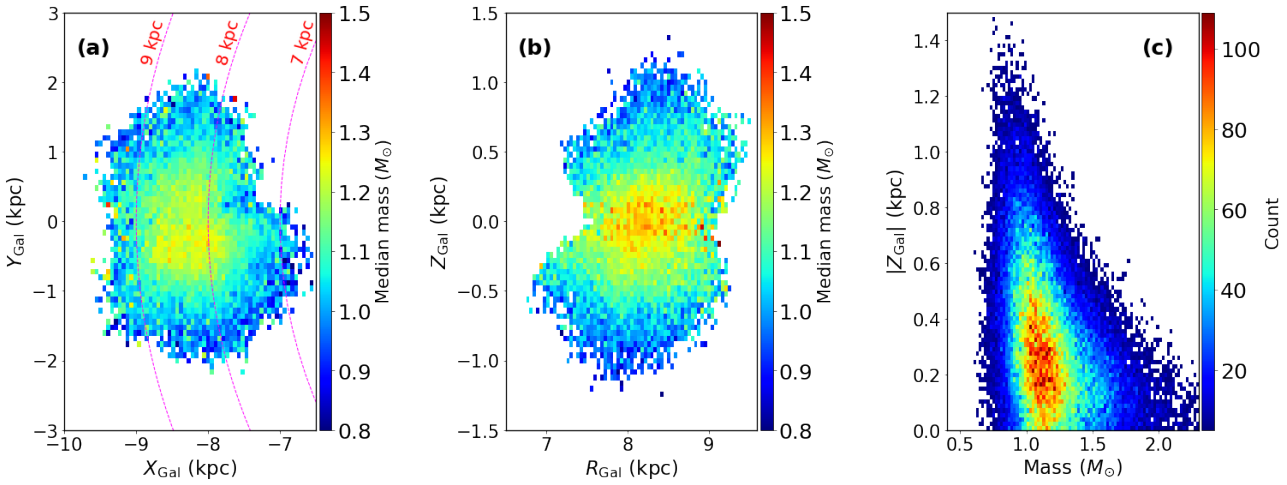

Figure 17. Spatial distribution of the low luminosity sample in Galactocentric coordinates. In each visualization, bins with fewer than 5 stars are not shown. (a) Position in Galactocentric Cartesian coordinates $(X_{\rm Gal}, Y_{\rm Gal})$. The coordinates are right-handed, such that the Sun is positioned at $(X_{\rm Gal,\odot}, Y_{\rm Gal,\odot}) = (-8.122, 0)$ kpc, with increasingly negative $X_{\rm Gal}$ indicating further distances from the Galactic center. The concentric lines indicate locations of constant radial distance from the Galactic center located at the origin. (b) Position in Galactocentric cylindrical coordinates $(R_{\rm Gal}, Z_{\rm Gal})$. (c) Distribution of masses as a function of vertical distance from the Galactic plane, $|Z_{\rm Gal}|$.

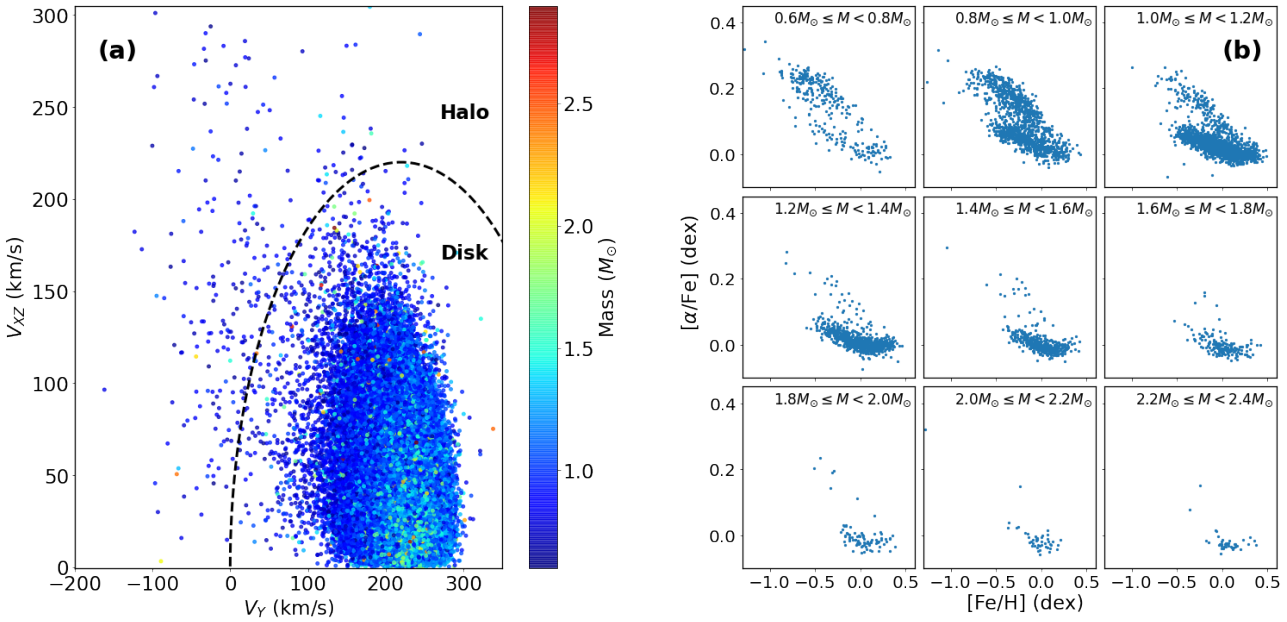

Figure 18. (Left) Toomre diagram of stars in the low luminosity sample with `ruwe` ≤ 1.40 and `mass_flag` $= 1$. The line corresponds to the boundary $|V - V_{\rm LSR}| > 220$ km/s that separates the halo and disk populations following Bonaca et al. (2017). $V_{\rm LSR}$ is assumed as (0, 220, 0) km/s in the Galactocentric Cartesian coordinate system (V_X, V_Y, V_Z). (Right) The [α/Fe]-[Fe/H] diagram of 4,858 stars in the low luminosity sample that have chemical abundances from APOGEE Data Release 16, with different panels corresponding to different mass bins.

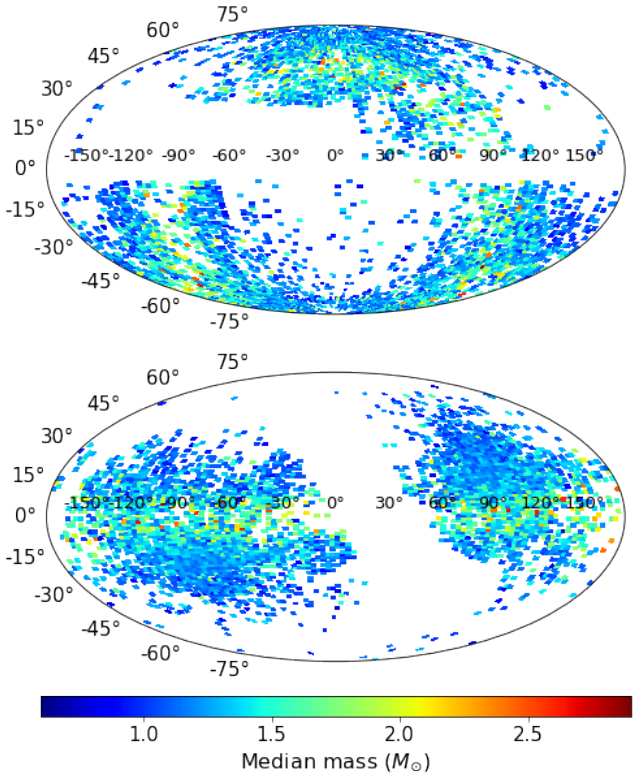

Figure 19. All-sky *Gaia*-asteroseismology mass map of stars in the high luminosity sample with `ruwe` ≤ 1.40 and `mass_flag` $= 1$ plotted in ecliptic coordinates in the top panel, and using the Galactic coordinate system (l, b) in the bottom panel. There are 100 bins across each dimension (longitude and latitude), with bins having fewer than 2 stars excluded.

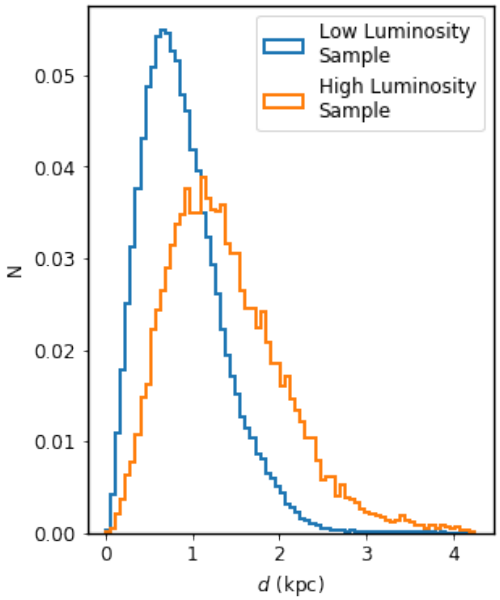

Figure 20. A comparison of distances between targets in the low luminosity sample with those in the high luminosity sample.

lowing Bonaca et al. (2017), we define $V_{\rm LSR} = (0, 220, 0)$ km/s and identify all stars with $|V - V_{\rm LSR} > 220|$ km/s as having velocities representative of populations in the Milky Way halo. Interestingly, we find ~ 240 stars with halo-like kinematics, which carries forward prospects of probing halo populations across the sky with TESS in future work.

Finally, Figure 18b shows the [α/Fe]-[Fe/H] relation for 4,858 stars in the low luminosity sample that have measured chemical abundances from APOGEE Data Release 16 (Majewski et al. 2017) of the Sloan Sky Digital Survey (Ahumada et al. 2020). The [α/Fe]-[Fe/H] relation is a frequently examined diagnostic in chemical evolution studies of the Milky Way disk (e.g., Adibekyan et al. 2011; Haywood et al. 2013; Bensby et al. 2014; Anders et al. 2017; Silva Aguirre et al. 2018), and distinguishes between young, low-α and old, high-α stellar populations. Under the assumption that mass is a proxy for stellar age, the trend shown by our seismic sample is consistent with the expected results whereby more massive stars (which are typically younger) have a greater tendency to populate the low-α regime in the diagram, which suggests the usefulness of our seismic yield for chemical evolution studies in large volumes of the Milky Way disk.

6.2. *High Luminosity Sample Results*

We display all-sky Hammer map projections of the high luminosity sample's seismic masses in Figure 19, where we find the same global trends in mass as a function of position, in particular the trend of higher masses within the Galactic plane. Compared to the low luminosity sample, the high luminosity sample typically probes farther distances as shown in Figure 20, which is expected given that it contains more low $\nu_{\rm max}$ giants at fainter magnitudes. However, Figure 21 shows that the spatial distribution of the sample is generally similar compared to that of the low luminosity sample in Figure 17. Finally, we examine the high luminosity sample's chemo-kinetical properties in Figure 22 and find similar global trends to those of the low luminosity sample in Figure 18 as well as $\sim$80 targets with halo-like kinematics. The broad similarity in results across samples gives us confidence the oscillations detected in the high luminosity sample are genuine despite differences in the methods applied to achieve the result.

7. CONCLUSIONS

We have presented the first all-sky sample of oscillating red giants using MIT Quick-Look Pipeline photom-

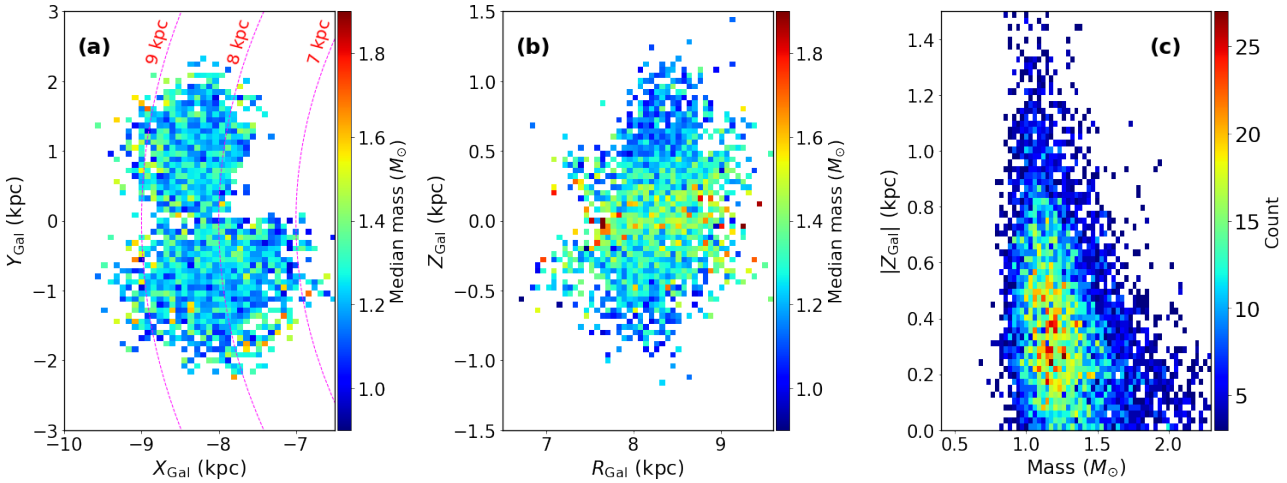

Figure 21. Same as Figure 17, but for the high luminosity sample.

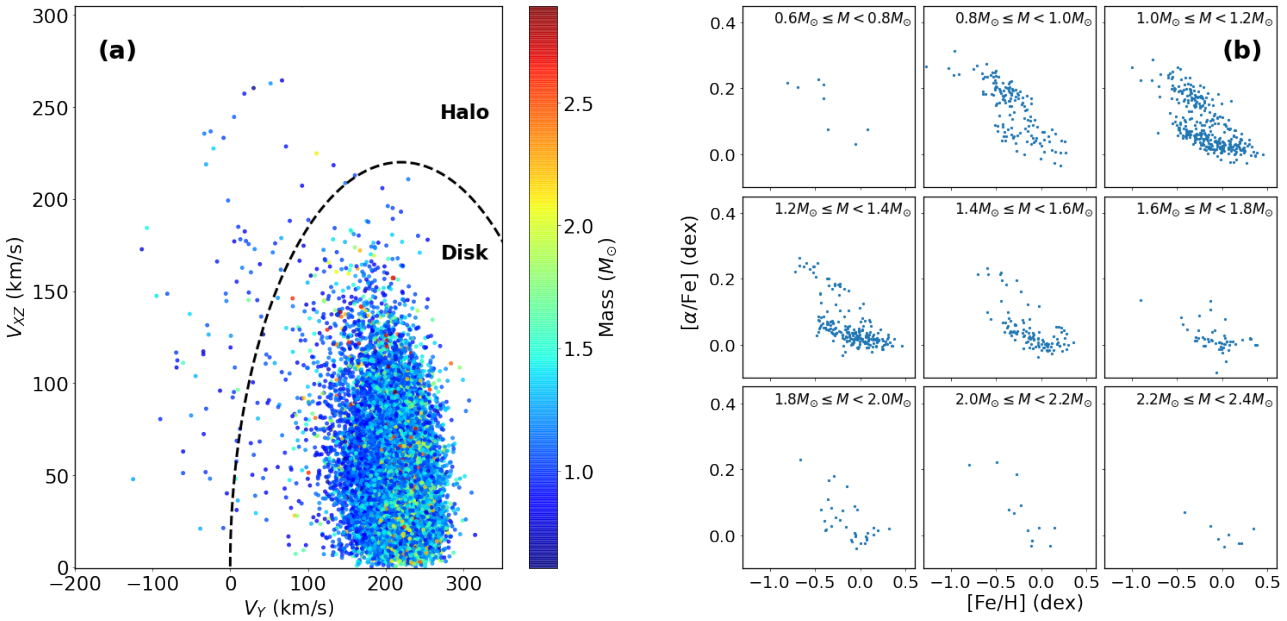

Figure 22. Same as Figure 18, but for the high luminosity sample. The right panel shows a total of 925 stars in the high luminosity sample with APOGEE DR16 chemical abundances.

etry of the first 26 sectors of TESS Full Frame Images. Our main results are summarized as follows:

- We reported red giant oscillations in a total of 129,323 targets from over 20 million light curves spanning TESS magnitudes as faint as 13.5. This yield comprises 113,187 low luminosity targets detected by our deep learning classifier that have frequencies at maximum power ($\nu_{\rm max}$) typically above 25μHz and 16,136 additional higher luminosity targets vetted using a combination of supervised and unsupervised learning techniques that have 10μHz $< \nu_{\rm max} \lesssim$ 25μHz .
- For each seismic detection, we reported estimates of its frequency at maximum power ($\nu_{\rm max}$), luminosity (L), radius (R), surface temperature ($T_{\rm eff}$), and distance (d). To produce a high quality target list of oscillating red giants, we have applied thresholds in our machine learning algorithms and applied statistical detection probabilities based on global SNR estimates to minimize the number of false positives. Our reported results are therefore that of an early detection yield and not that of a complete survey of all underlying oscillating giants from TESS Full Frame Images. Because we recovered ∼130,000 unique oscillating giants despite our

conservative vetting measures, the lack of optimal light curve corrections required for asteroseismology, and the use of only one month-long observations, it is reasonable to expect that the number of targets in our reported detection yield is a lower bound to the complete oscillating red giant yield from TESS's nominal mission.

- With our detection yield we demonstrated the enormous potential of TESS for all-sky Galactic archeology by presenting the first ever all-sky *Gaia*-asteroseismology mass map that displays expected broad astrophysical trends in mass across the sky. With data from the Quick-Look Pipeline limited to a TESS magnitude of 13.5, we found our yield to typically span distances within 1 kpc. Despite most stars located relatively near to us, they sample a sufficiently large volume of space that appear promising in probing the mass structure of the Milky Way disk. We additionally found over 300 targets with velocities representative of stars in the Galactic halo. Finally, by assuming mass as an age proxy for giants, we showed that a subset of our sample with APOGEE elemental abundances displays the expected trend of [α/Fe]-[Fe/H] with age.

Our 'quick look' at the all-sky asteroseismic yield from TESS has notably provided us insights on how to improve our data and methodology for further work to expand the yield across Full Frame Images. Currently, we have used only 'raw' data from the Quick-Look Pipeline, which lack detrending to remove instrumental noise. Upcoming data releases from the TESS Asteroseismic Science Consortium (e.g., Handberg et al. 2021) will provide light curves with instrumental noise corrections that are optimized for asteroseismology for all FFI targets up to a TESS magnitude of 15, which will significantly increase the detection yield across all TESS sectors. Another vital insight is the need for improved machine learning algorithms and training data. As the asteroseismic analyses of TESS data further progresses across the scientific community, it will become possible to use or develop training data that is more representative of real TESS FFI observations. The availability of better training data will subsequently facilitate improvements with our deep learning algorithms, particularly in the detection of oscillations for the faintest and most luminous targets from TESS. These future prospects, when combined with TESS's potential for all-sky Galactic studies, will certainly provide a more complete and detailed view of the Milky Way.

Funding for the TESS mission is provided by the NASA Explorer Program. M.H. acknowledges support from NASA through the NASA Hubble Fellowship grant HST-HF2-51459.001 awarded by the Space Telescope Science Institute, which is operated by the Association of Universities for Research in Astronomy, Incorporated, under NASA contract NAS5-26555. D.H. acknowledges support from the Alfred P. Sloan Foundation, the National Aeronautics and Space Administration (80NSSC21K0652), and the National Science Foundation (AST-1717000). JT acknowledges support for this work was provided by NASA through the NASA Hubble Fellowship grant #51424 awarded by the Space Telescope Science Institute, which is operated by the Association of Universities for Research in Astronomy, Inc., for NASA, under contract NAS5-26555 and by NASA Award 80NSSC20K0056. JCZ is supported by an NSF Astronomy and Astrophysics Postdoctoral Fellowship under award AST-2001869.

Software: Astropy (Astropy Collaboration et al. 2018), `isoclassify` (Huber et al. 2017; Berger et al. 2020), `MiniSom` (Vettigli 2018), Pytorch (Paszke et al. 2019)

APPENDIX

A. NETWORK ARCHITECTURE

Tables 1A and 1B detail the structure of the classifier and the regression network, respectively. The networks are developed using the Pytorch version 1.1.0 deep learning library (Paszke et al. 2019). The networks are trained using the Adam optimizer (Kingma & Ba 2014) with an initial learning rate of 0.0001 and early stopping applied.

The networks are generally similar to those implemented by Hon et al. (2018b), with a few key differences. First, both networks have dropout applied only to the final feature extraction layer, with a small dropout probability of 0.1. Because this current work has significantly more training data compared to the *Kepler*-as-*K2* used by Hon et al. (2018b), weaker regularization is required to prevent network overfitting. The second difference relates to the uncertainty estimation of the $\nu_{\rm max}$ regression network. The previous study uses Monte Carlo dropout (Gal &

Table 1A. Structure of the classifier to detect oscillating red giants from images of power spectra.

Component	Layer	Filter Size	Output Shape
Feature Extraction	`conv1`[b]	(5,5)	(128,128,4)
	`pool1`	(2,2)	(64,64,4)
	`conv2`	(3,3)	(64,64,8)
	`pool2`	(2,2)	(32,32,8)
	`conv3`	(3,3)	(32,32,16)
	`pool3`	(2,2)	(16,16,16)
	`flatten`	-	(4096,)
	`drop`[c]	-	(4096,)
Class Score Estimation	`dense1`	(4096,128)	(128,)
	`output`	(128,1)	(1,)

NOTE—The rectified linear unit activation (Nair & Hinton 2010, ReLU) is applied after every `conv` and `dense` layer.
[a] For convolutional layers, this column corresponds to the dimensions of the convolving kernel, whereas for dense layers the column corresponds to (`number of neurons in previous layer`, `number of neurons in current layer`).
[b] For convolutional layers, weight shapes are in format (number of filters, receptive field size), while output shapes are in format (height, width, number of filters).
[c] We implement regular Dropout (Hinton et al. 2012; Srivastava et al. 2014) with a drop probability of 0.1.

Ghahramani 2016), while our work in this study explicitly estimates $\sigma_{\nu_{\rm max}}$ through an auxiliary output layer (e.g., Kendall & Gal 2017). Consequently, optimizing the $\nu_{\rm max}$ regression network is not done by minimizing the mean squared error (as before), but the negative log-likelihood, E, given by the following:

$$p(y \mid \mathbf{x}) = \frac{1}{(2\pi)^{1/2}\sigma(\mathbf{x})} \exp\left(-\frac{(y-\nu_{\rm max,pred})^2}{2\sigma(\mathbf{x})^2}\right), \tag{A1}$$

$$E = \sum_{m=1}^{m_{\rm tot}} -\ln p(y_m \mid \mathbf{x}_m). \tag{A2}$$

Here, $\mathbf{x}$ is the input image, $\sigma(\mathbf{x})$ is $\sigma_{\nu_{\rm max}}$, y is the ground truth value of $\nu_{\rm max}$, $\nu_{\rm max,pred}$ is the estimated value of the frequency at maximum power by the $\nu_{\rm max}$ regression network, and $m_{\rm tot}$ is total number of power spectra in the training set.

B. `CELERITE` POWER SPECTRA

Figure 23 shows example power spectra of oscillating red giants generated by `celerite` compared to real TESS giants with the same $\nu_{\rm max}$ and TESS magnitudes. There are notable differences between the noise levels of real and simulated data, which as discussed in the main text is the result of the latter data not including noise contributions from instrumental sources or flux contamination. Additionally, in the absence of such contributions, the frequency-power profile of the simulated power spectra appear different to that of the real data, particularly at low frequencies. Future work will include more realistic simulations; however, the current data are sufficient to benchmark the network

Table 1B. Structure of the regression network to estimate $\nu_{\rm max}$ from images of power spectra showing red giant oscillations.

Component	Layer	Filter Size	Output Shape
Feature Extraction	`conv1`[b]	(5,5)	(128,128,4)
	`pool1`	(2,2)	(64,64,4)
	`conv2`	(3,3)	(64,64,8)
	`pool2`	(2,2)	(32,32,8)
	`conv3`	(3,3)	(32,32,16)
	`pool3`	(2,2)	(16,16,16)
	`flatten`	-	(4096,)
	`drop`[c]	-	(4096,)
Mean Value Estimation	`dense1a`	(4096,256)	(256,)
	`dense2a`	(256,256)	(256,)
	`output` $\nu_{\rm max}$	(256,1)	(1,)
Uncertainty Estimation	`dense1b`	(4096,256)	(256,)
	`dense2b`	(256,256)	(256,)
	`output` $\sigma_{\nu_{\rm max}}$	(256,1)	(1,)

NOTE—The rectified linear unit activation (Nair & Hinton 2010, ReLU) is applied after every `conv` and `dense` layer.
[a] For convolutional layers, this column corresponds to the dimensions of the convolving kernel, whereas for dense layers the column corresponds to (`number of neurons in previous layer`, `number of neurons in current layer`).
[b] For convolutional layers, weight shapes are in format (number of filters, receptive field size), while output shapes are in format (height, width, number of filters).
[c] We implement regular Dropout (Hinton et al. 2012; Srivastava et al. 2014) with a drop probability of 0.1.

trained on *Kepler*-as-TESS data (Section 3.3) and to train a new regressor to estimate the $\nu_{\rm max}$ values for the high luminosity sample (Section 4.2.2).

C. FAINT AND LUMINOUS GIANTS

Figure 24 shows power spectra of two known oscillating red giants from the *Kepler* field and illustrates the difficulty in identifying the oscillation power excess for stars with low $\nu_{\rm max}$. In particular, the oscillation power envelope for such stars are dispersed across relatively few frequency bins and may have amplitudes only marginally above other low frequency systematic noise. For stars brighter in TESS magnitude, for which the granulation background is still visible, the power excess above the background produces a distinctive 'knee'-like profile in the power spectrum. For fainter stars in which white noise dominates their power spectra, the lack of such a curvature makes it difficult to distinguish oscillation peaks from white noise except for those with particularly large oscillation amplitudes (e.g., right panel in Figure 24).

D. EXAMPLES OF OSCILLATING GIANTS IN FINAL YIELD

We show several examples of oscillating red giants from the low luminosity sample in Figure 25, and examples from the high luminosity sample in Figure 26.

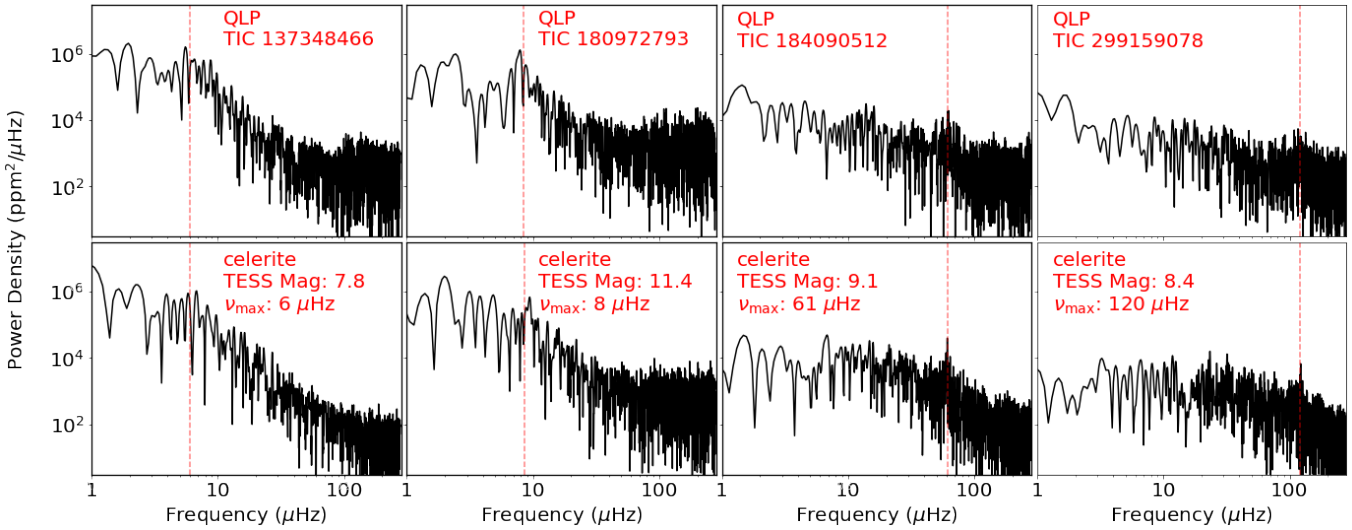

Figure 23. A comparison of real TESS power spectra (top row) with synthetic power spectra (bottom row) generated by `celerite` in this work. Each row corresponds to a red giant with a particular TESS magnitude that is oscillating at a specific $\nu_{\rm max}$.

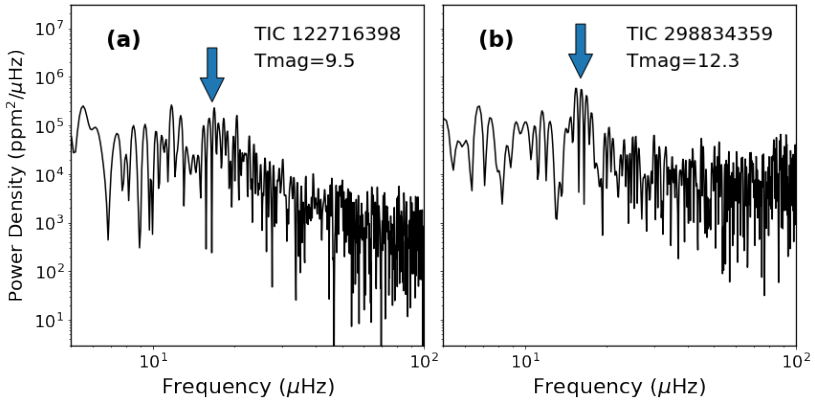

Figure 24. Power spectra for TESS FFI targets that are known to be luminous, oscillating *Kepler* red giants from the work by Yu et al. (2020). The blue arrows indicate $\nu_{\rm max}$, while Tmag indicates TESS magnitude. TIC 122716398 in panel (a) is a bright and luminous giant, while TIC 298834359 in panel (b) is much fainter but still has a visible power excess due to its particularly large oscillation amplitude, i.e. $\sim 370\mu$mag at $\nu_{\rm max} \sim 15\mu$Hz (Yu et al. 2020, their Figure 2a).

E. SELF-ORGANIZING MAP

A self-organizing map (SOM) applies competitive learning between neurons to learn a topographic map to produce a low dimensional, discretized representation of the input space. Training a SOM typically requires specifying *a priori* the number of neurons, n, to represent the map, where each neuron has its associated weight vector w_n that has a matching dimensionality to the input space.

Training a SOM proceeds by first initializing w_n randomly, followed by performing iterations of the following steps (with each iteration denoted by t):

1. Randomly sample an input $\mathbf{x}$ from the dataset.
2. Determine $\underset{k}{\rm argmin}\, d(w_k, \mathbf{x})$ i.e., the closest matching neuron to $\mathbf{x}$. The function d is a distance measure between two arrays; here we adopt the Euclidean distance.
3. Update the weights of all n neurons with the following:
   $w_n \leftarrow w_n \cdot \eta(t) \cdot h(k) \cdot (\mathbf{x} - w_n)$

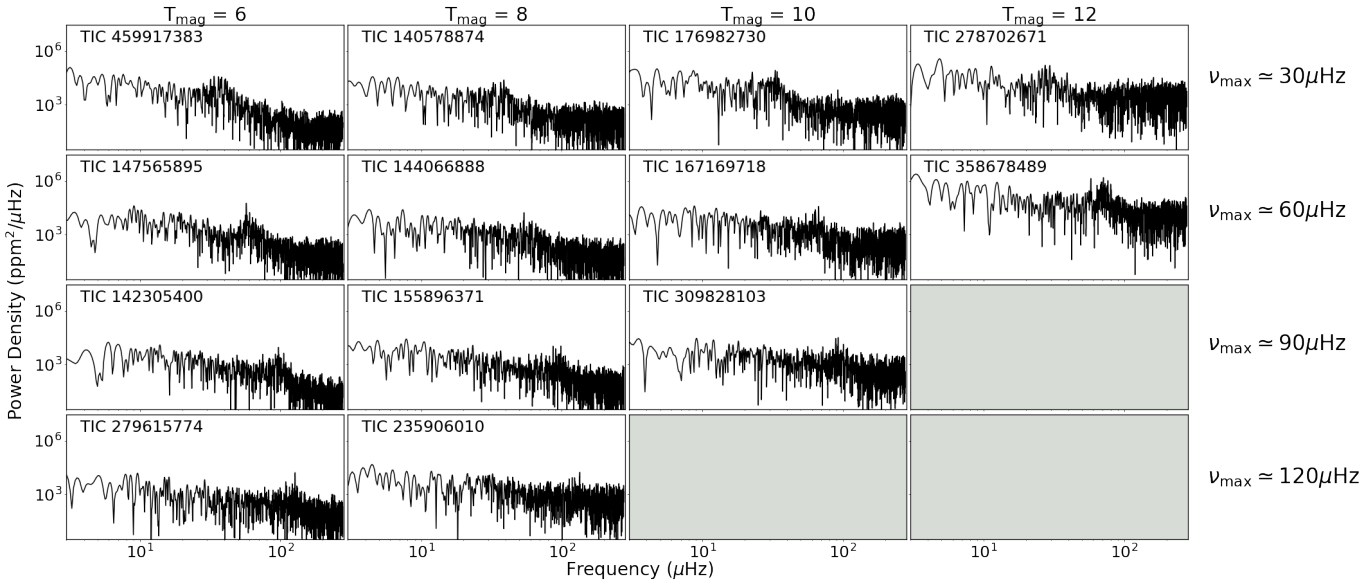

Figure 25. Examples of oscillating giants from the low luminosity sample. Each row corresponds to a particular $\nu_{\rm max}$ value, while each column corresponds to a specific TESS magnitude. The bottom right panels are greyed out because no oscillating giants are found with such values of $\nu_{\rm max}$ and TESS magnitudes in our sample as a consequence of the oscillation detection limit (Figure 8b).

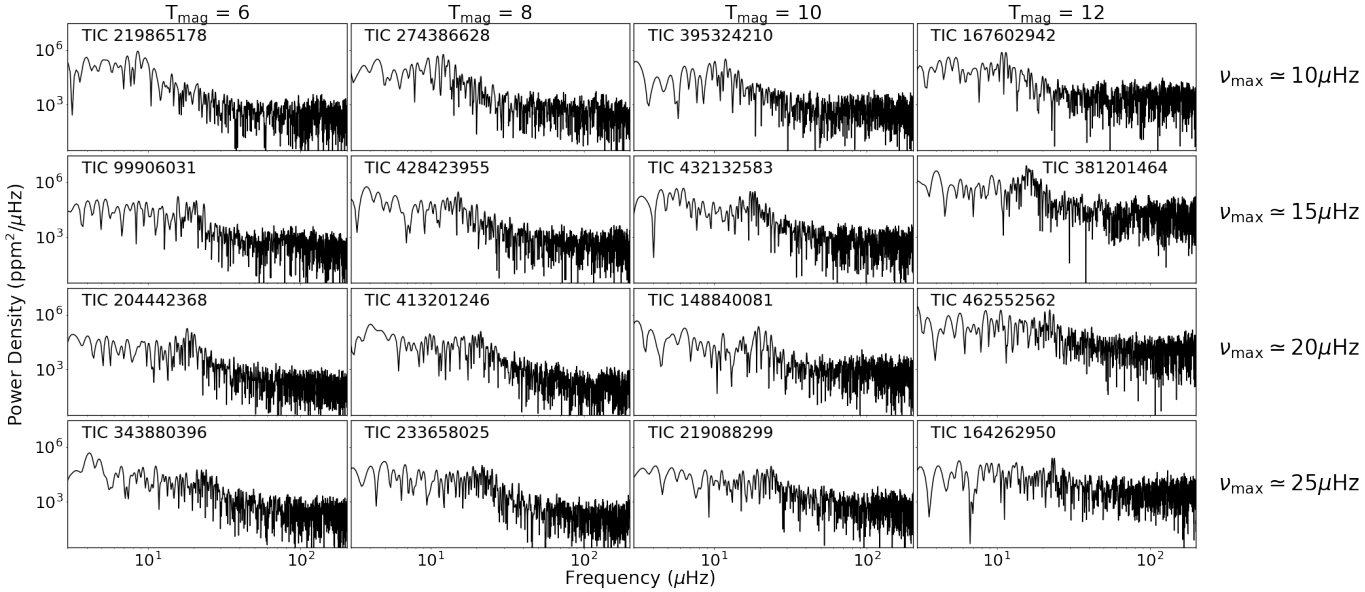

Figure 26. Same as Figure 25, but for oscillating giants in the high luminosity sample.

The function $\eta(t)$ determines the learning rate of the updates to the SOM and decays as a function of t:

$$\eta(t) = \frac{\lambda}{1 + t/0.5t_{\rm max}}, \tag{E3}$$

where λ is the initial learning rate and $t_{\rm max}$ is the maximum number of iterations to train the SOM. We use $\lambda = 0.1$ and $t_{\rm max} = 30{,}000$. The function $h(k)$ is the neighbourhood function that determines the spatial influence of a neuron update on the grid. Typically, $h(k)$ takes the form of a Gaussian parameterized by a width σ that is centered on neuron k (the best matching neuron for an input), such that w_n for adjacent neurons are updated the most, while those of neurons farther away receiving smaller updates. However, we find that for assigning spectra into spatially

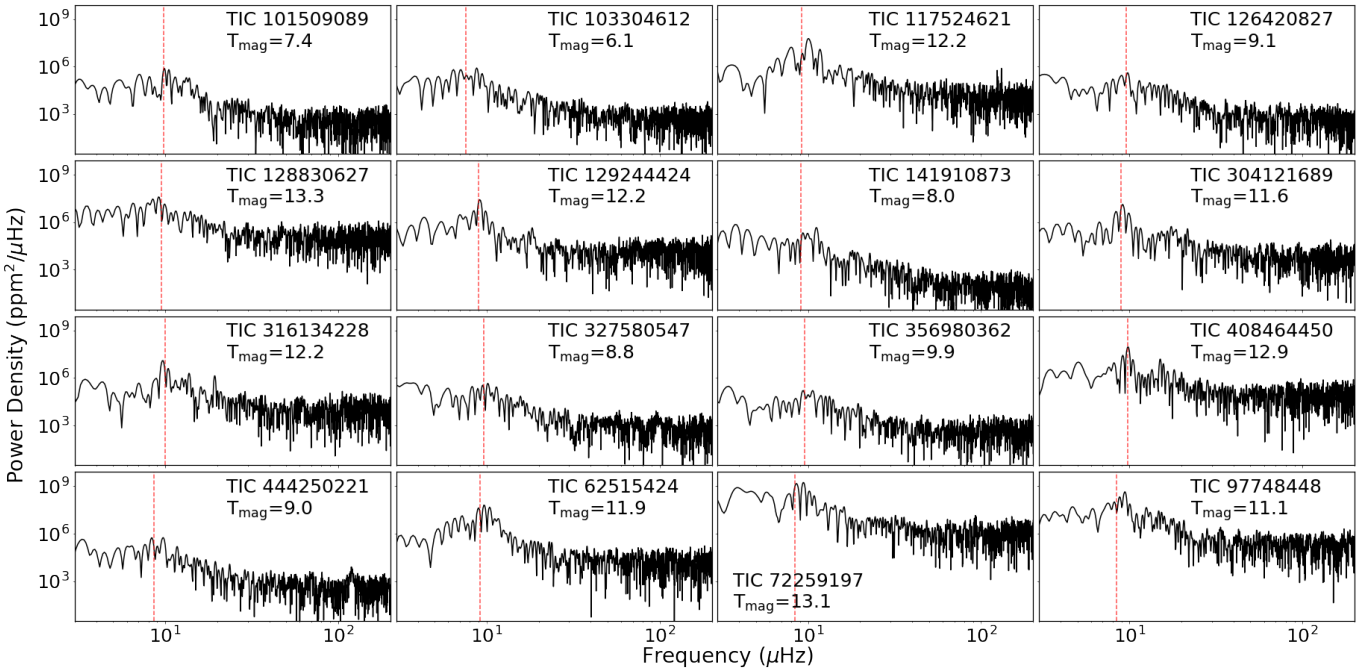

Figure 27. Examples of power spectra for luminous targets with variability at frequencies $\lesssim 10\mu$Hz in the power spectra. The red lines indicate the estimated frequency at maximum power of the signals corresponding to such variability.

correlated regions in the map in our work (Figure 10), a 'bubble' neighbourhood function with a width of 2 works well, i.e., $h(k) = 1$ for neurons within the coordinate range $(i-2, j-2)$ to $(i+2, j+2)$, where (i, j) are the coordinates of neuron k on the 2D map.

Each input x is assigned to different neurons, depending on which neuron has w_n that is smallest in Euclidean distance to the input. The difference in distance between x and w_n is denoted as the quantization error. The average quantization error over all samples assigned to a neuron is a useful quantity for measuring the convergence of the SOM and the quality of the mapping. A low quantization error indicates that the neuron weight vector forms a template that matches power spectra assigned to that neuron well. We tune the size of the SOM and its parameters λ, $t_{\max}$, $h(k)$ to minimize the average quantization error.

F. VERY LUMINOUS TARGETS FROM HIGH LUMINOSITY SAMPLE

Table 1C lists a total of 2,457 TESS targets whose power spectra show peaks at frequencies less than 10μHz. As discussed in Section 4.2, the type of variability giving rise to such peaks is difficult to confirm for each target despite having giant-like R and $T_{\rm eff}$. Figure 27 shows examples of power spectra for these targets, which highlights the ambiguity of resolving the variability type for these stars.

REFERENCES

Adibekyan, V. Z., Santos, N. C., Sousa, S. G., & Israelian, G. 2011, A&A, 535, L11, doi: 10.1051/0004-6361/201118240

Ahumada, R., Prieto, C. A., Almeida, A., et al. 2020, ApJS, 249, 3, doi: 10.3847/1538-4365/ab929e

Anders, F., Chiappini, C., Rodrigues, T. S., et al. 2017, A&A, 597, A30, doi: 10.1051/0004-6361/201527204

Armstrong, D. J., Kirk, J., Lam, K. W. F., et al. 2016, Monthly Notices of the Royal Astronomical Society, 456, 2260

Astraatmadja, T. L., & Bailer-Jones, C. A. L. 2016, ApJ, 832, 137, doi: 10.3847/0004-637X/832/2/137

Astropy Collaboration, Price-Whelan, A. M., Sipőcz, B. M., et al. 2018, AJ, 156, 123, doi: 10.3847/1538-3881/aabc4f

Table 1C. A list of 2,457 luminous TESS targets with an estimated $\nu_{\rm max} < 10\mu$Hz that are not included in our final yield. For these stars, $\nu_{\rm max}$ may not necessarily correspond to oscillation frequencies, but is nonetheless the frequency at which a maximum in power is found in the power spectrum. The other columns are defined similarly to Tables 1 and 2. The full version of this table is available in a machine-readable format as supplementary material in the online journal, with a portion shown here for guidance regarding its form and content.

TIC	$\nu_{\rm max}$ (μHz)	Tmag (mag)	$T_{\rm eff}$ (K)	R ($R_\odot$)	L ($L_\odot$)	d (kpc)	ruwe	mass_flag
136419	8.4 ± 0.2	10.4	4462 ± 89	19.9 ± 1.0	140.5 ± 8.9	1.648 ± 0.046	0.92	1
31769257	9.5 ± 0.5	9.9	4226 ± 84	25.6 ± 2.4	187.9 ± 31.2	1.641 ± 0.132	3.77	1
73440430	8.3 ± 0.4	5.2	4151 ± 83	28.5 ± 3.8	216.3 ± 54.7	0.225 ± 0.005	4.53	1
289057515	7.6 ± 0.3	10.6	4544 ± 90	23.6 ± 1.4	212.7 ± 19.0	2.182 ± 0.090	1.01	1
411418366	7.6 ± 0.1	13.1	4461 ± 89	16.3 ± 1.3	94.3 ± 12.9	4.457 ± 0.294	1.04	0
...	...	...	...	...	...	...	...	...

Baglin, A., Auvergne, M., Boisnard, L., et al. 2006, in COSPAR Meeting, Vol. 36, 36th COSPAR Scientific Assembly

Bailer-Jones, C. A. L. 2015, PASP, 127, 994, doi: 10.1086/683116

Belkacem, K., Goupil, M. J., Dupret, M. A., et al. 2011, A&A, 530, A142, doi: 10.1051/0004-6361/201116490

Bellinger, E. P. 2020, MNRAS, 492, L50, doi: 10.1093/mnrasl/slz178

Belokurov, V., Penoyre, Z., Oh, S., et al. 2020, MNRAS, 496, 1922, doi: 10.1093/mnras/staa1522

Bensby, T., Feltzing, S., & Oey, M. S. 2014, A&A, 562, A71, doi: 10.1051/0004-6361/201322631

Berger, T. A., Huber, D., Gaidos, E., van Saders, J. L., & Weiss, L. M. 2020, AJ, 160, 108, doi: 10.3847/1538-3881/aba18a

Bonaca, A., Conroy, C., Wetzel, A., Hopkins, P. F., & Kereš, D. 2017, ApJ, 845, 101, doi: 10.3847/1538-4357/aa7d0c

Borucki, W. J., Koch, D., Basri, G., et al. 2010, Science, 327, 977, doi: 10.1126/science.1185402

Bovy, J., Rix, H.-W., Green, G. M., Schlafly, E. F., & Finkbeiner, D. P. 2016, ApJ, 818, 130, doi: 10.3847/0004-637X/818/2/130

Brown, T. M., Gilliland, R. L., Noyes, R. W., & Ramsey, L. W. 1991, ApJ, 368, 599, doi: 10.1086/169725

Bugnet, L., García, R. A., Mathur, S., et al. 2019, A&A, 624, A79, doi: 10.1051/0004-6361/201834780

Campante, T. L., Schofield, M., Kuszlewicz, J. S., et al. 2016, The Astrophysical Journal, 830, 138, doi: 10.3847/0004-637x/830/2/138

Casagrande, L., Silva Aguirre, V., Schlesinger, K. J., et al. 2016, MNRAS, 455, 987, doi: 10.1093/mnras/stv2320

Chaplin, W. J., Kjeldsen, H., Bedding, T. R., et al. 2011, The Astrophysical Journal, 732, 54, doi: 10.1088/0004-637x/732/1/54

Choi, J., Dotter, A., Conroy, C., et al. 2016, ApJ, 823, 102, doi: 10.3847/0004-637X/823/2/102

de Assis Peralta, R., Samadi, R., & Michel, E. 2018, Astronomische Nachrichten, 339, 134, doi: 10.1002/asna.201813469

Ding, P.-J., Zhu, Z., & Liu, J.-C. 2019, Research in Astronomy and Astrophysics, 19, 068, doi: 10.1088/1674-4527/19/5/68

Drimmel, R., Cabrera-Lavers, A., & López-Corredoira, M. 2003, A&A, 409, 205, doi: 10.1051/0004-6361:20031070

Elsworth, Y., Hekker, S., Johnson, J. A., et al. 2019, MNRAS, 489, 4641, doi: 10.1093/mnras/stz2356

Evans, D. F. 2018, Research Notes of the American Astronomical Society, 2, 20, doi: 10.3847/2515-5172/aac173

Gaia Collaboration, Brown, A. G. A., Vallenari, A., et al. 2020, arXiv e-prints, arXiv:2012.01533. https://arxiv.org/abs/2012.01533

Gal, Y., & Ghahramani, Z. 2016, in Proceedings of the 33rd International Conference on International Conference on Machine Learning - Volume 48, ICML'16 (JMLR.org), 1050–1059

González Hernández, J. I., & Bonifacio, P. 2009, A&A, 497, 497, doi: 10.1051/0004-6361/200810904

Green, G. M., Schlafly, E., Zucker, C., Speagle, J. S., & Finkbeiner, D. 2019, ApJ, 887, 93, doi: 10.3847/1538-4357/ab5362

Handberg, R., Buzasi, D. L., & Lund, M. N. 2021, T'DA Data Release Notes - Data Release 5 for TESS Sectors 1-6, doi: 10.5281/zenodo.4549083

Haywood, M., Di Matteo, P., Lehnert, M. D., Katz, D., & Gómez, A. 2013, A&A, 560, A109, doi: 10.1051/0004-6361/201321397

Hinton, G. E., Srivastava, N., Krizhevsky, A., Sutskever, I., & Salakhutdinov, R. R. 2012, ArXiv e-prints. https://arxiv.org/abs/1207.0580

Hon, M., Stello, D., Sharma, S., et al. 2019, doi: 10.1093/mnras/stz622

Hon, M., Stello, D., & Yu, J. 2018a, Monthly Notices of the Royal Astronomical Society, 476, 3233, doi: 10.1093/mnras/sty483

Hon, M., Stello, D., & Zinn, J. C. 2018b, The Astrophysical Journal, 859, 64, doi: 10.3847/1538-4357/aabfdb

Howell, S. B., Sobeck, C., Haas, M., et al. 2014, Publications of the Astronomical Society of the Pacific, 126, 398

Huang, C. X., Vanderburg, A., Pál, A., et al. 2020a, Research Notes of the American Astronomical Society, 4, 204, doi: 10.3847/2515-5172/abca2e

—. 2020b, Research Notes of the American Astronomical Society, 4, 206, doi: 10.3847/2515-5172/abca2d

Huber, D., Bedding, T. R., Stello, D., et al. 2011, ApJ, 743, 143, doi: 10.1088/0004-637X/743/2/143

Huber, D., Zinn, J., Bojsen-Hansen, M., et al. 2017, ApJ, 844, 102, doi: 10.3847/1538-4357/aa75ca

Jenkins, J. M., Caldwell, D. A., Chandrasekaran, H., et al. 2010, The Astrophysical Journal, 713, L120, doi: 10.1088/2041-8205/713/2/l120

Kallinger, T., De Ridder, J., Hekker, S., et al. 2014, A&A, 570, A41, doi: 10.1051/0004-6361/201424313

Kendall, A., & Gal, Y. 2017, What Uncertainties Do We Need in Bayesian Deep Learning for Computer Vision?

Kgoadi, R., Engelbrecht, C., Whittingham, I., & Tkachenko, A. 2019, arXiv e-prints, arXiv:1906.06628. https://arxiv.org/abs/1906.06628

Kingma, D. P., & Ba, J. 2014, ArXiv e-prints

Kjeldsen, H., & Bedding, T. R. 1995, A&A, 293, 87. https://arxiv.org/abs/astro-ph/9403015

Kohonen, T. 1982, Biological Cybernetics, 43, 59, doi: 10.1007/bf00337288

Kuszlewicz, J. S., Hekker, S., & Bell, K. J. 2020, MNRAS, 497, 4843, doi: 10.1093/mnras/staa2155

Lindegren, L. 2018. http://www.rssd.esa.int/doc_fetch.php?id=3757412

Lindegren, L., Klioner, S. A., Hernández, J., et al. 2020, arXiv e-prints, arXiv:2012.03380. https://arxiv.org/abs/2012.03380

Lomb, N. R. 1976, Ap&SS, 39, 447, doi: 10.1007/BF00648343

Mackereth, J. T., Bovy, J., Schiavon, R. P., et al. 2017, MNRAS, 471, 3057, doi: 10.1093/mnras/stx1774

Mackereth, J. T., Miglio, A., Elsworth, Y., et al. 2021, MNRAS, doi: 10.1093/mnras/stab098

Majewski, S. R., Schiavon, R. P., Frinchaboy, P. M., et al. 2017, The Astronomical Journal, 154, 94, doi: 10.3847/1538-3881/aa784d

Marshall, D. J., Robin, A. C., Reylé, C., Schultheis, M., & Picaud, S. 2006, A&A, 453, 635, doi: 10.1051/0004-6361:20053842

Mathur, S., García, R. A., Huber, D., et al. 2016, ApJ, 827, 50, doi: 10.3847/0004-637X/827/1/50

Mathur, S., Santos, u., & García, R. A. 2019, Kepler Light Curves Optimized For Asteroseismology ("KEPSEISMIC"), STScI/MAST, doi: 10.17909/t9-mrpw-gc07

Miglio, A. 2011, in Red Giants as Probes of the Structure and Evolution of the Milky Way (Springer Berlin Heidelberg), 11–21, doi: 10.1007/978-3-642-18418-5_2

Miglio, A., Chiappini, C., Morel, T., et al. 2013, MNRAS, 429, 423, doi: 10.1093/mnras/sts345

Miglio, A., Chiappini, C., Mackereth, J. T., et al. 2021, A&A, 645, A85, doi: 10.1051/0004-6361/202038307

Mosser, B., Gehan, C., Belkacem, K., et al. 2018, A&A, 618, A109, doi: 10.1051/0004-6361/201832777

Mosser, B., Belkacem, K., Goupil, M. J., et al. 2011, A&A, 525, L9, doi: 10.1051/0004-6361/201015440

Mosser, B., Elsworth, Y., Hekker, S., et al. 2012, A&A, 537, A30, doi: 10.1051/0004-6361/201117352

Nair, V., & Hinton, G. E. 2010, in Proceedings of the 27th International Conference on Machine Learning (ICML-10), ed. J. Fürnkranz & T. Joachims (Omnipress), 807–814

Paszke, A., Gross, S., Massa, F., et al. 2019, in Advances in Neural Information Processing Systems 32, ed. H. Wallach, H. Larochelle, A. Beygelzimer, F. dAlché-Buc, E. Fox, & R. Garnett (Curran Associates, Inc.), 8024–8035

Pereira, F., Campante, T. L., Cunha, M. S., et al. 2019, MNRAS, 489, 5764, doi: 10.1093/mnras/stz2405

Pinsonneault, M. H., Elsworth, Y. P., Tayar, J., et al. 2018, ApJS, 239, 32, doi: 10.3847/1538-4365/aaebfd

Prša, A., Harmanec, P., Torres, G., et al. 2016, AJ, 152, 41, doi: 10.3847/0004-6256/152/2/41

Rendle, B. M., Miglio, A., Chiappini, C., et al. 2019, MNRAS, 490, 4465, doi: 10.1093/mnras/stz2454

Ricker, G. R., Winn, J. N., Vanderspek, R., et al. 2014, Journal of Astronomical Telescopes, Instruments, and Systems, 1, 014003, doi: 10.1117/1.jatis.1.1.014003

Rodrigues, T. S., Girardi, L., Miglio, A., et al. 2014, MNRAS, 445, 2758, doi: 10.1093/mnras/stu1907

Sanders, J. L., & Das, P. 2018, MNRAS, 481, 4093, doi: 10.1093/mnras/sty2490

Scargle, J. D. 1982, ApJ, 263, 835, doi: 10.1086/160554

Schofield, M., Chaplin, W. J., Huber, D., et al. 2019, The Astrophysical Journal Supplement Series, 241, 12, doi: 10.3847/1538-4365/ab04f5

Sharma, S., Stello, D., Bland-Hawthorn, J., et al. 2019, MNRAS, 490, 5335, doi: 10.1093/mnras/stz2861

Silva Aguirre, V., Bojsen-Hansen, M., Slumstrup, D., et al. 2018, MNRAS, 475, 5487, doi: 10.1093/mnras/sty150

Silva Aguirre, V., Stello, D., Stokholm, A., et al. 2020, ApJL, 889, L34, doi: 10.3847/2041-8213/ab6443

Srivastava, N., Hinton, G., Krizhevsky, A., Sutskever, I., & Salakhutdinov, R. 2014, J. Mach. Learn. Res., 15, 1929

Stello, D., Zinn, J., Elsworth, Y., et al. 2017, ApJ, 835, 83, doi: 10.3847/1538-4357/835/1/83

Sullivan, P. W., Winn, J. N., Berta-Thompson, Z. K., et al. 2015, The Astrophysical Journal, 809, 77, doi: 10.1088/0004-637x/809/1/77

Venn, K. A., Irwin, M., Shetrone, M. D., et al. 2004, AJ, 128, 1177, doi: 10.1086/422734

Vettigli, G. 2018, MiniSom: minimalistic and NumPy-based implementation of the Self Organizing Map. https://github.com/JustGlowing/minisom/

Vrard, M., Mosser, B., & Samadi, R. 2016, A&A, 588, A87, doi: 10.1051/0004-6361/201527259

Xiang, M., Liu, X., Shi, J., et al. 2017, ApJS, 232, 2, doi: 10.3847/1538-4365/aa80e4

Yu, J., Bedding, T. R., Stello, D., et al. 2020, MNRAS, 493, 1388, doi: 10.1093/mnras/staa300

Yu, J., Huber, D., Bedding, T. R., et al. 2018, The Astrophysical Journal Supplement Series, 236, 42, doi: 10.3847/1538-4365/aaaf74

Zinn, J. C. 2021, arXiv e-prints, arXiv:2101.07252. https://arxiv.org/abs/2101.07252

Zinn, J. C., Stello, D., Elsworth, Y., et al. 2020, ApJS, 251, 23, doi: 10.3847/1538-4365/abbee3